

JOURNAL OF GLACIOLOGY



CAMBRIDGE
UNIVERSITY PRESS

THIS MANUSCRIPT HAS BEEN SUBMITTED TO THE JOURNAL OF GLACIOLOGY AND HAS NOT BEEN PEER-REVIEWED.

Water flow through sediments and at the ice-sediment interface beneath Sermeq Kujalleq (Store Glacier), Greenland

Journal:	<i>Journal of Glaciology</i>
Manuscript ID	JOG-21-0085
Manuscript Type:	Article
Date Submitted by the Author:	25-Jun-2021
Complete List of Authors:	Doyle, Samuel; Aberystwyth University, Centre for Glaciology, Department of Geography and Earth Sciences Hubbard, Bryn; Aberystwyth University, Centre for Glaciology, Department of Geography & Earth Sciences Christoffersen, Poul; University of Cambridge, Scott Polar Research Institute Law, Robert; University of Cambridge, Scott Polar Research Institute Hewitt, Duncan; University College London, Department of Mathematics Neufeld, Jerome; University of Cambridge, Institute of Theoretical Geophysics, Department of Applied Mathematics and Theoretical Physics; University of Cambridge, BP Institute; University of Cambridge, Department of Earth Sciences, Bullard Laboratories Schoonman, Charlotte; University of Cambridge, Scott Polar Research Institute Chudley, Thomas ; University of Cambridge Scott Polar Research Institute Bougamont, Marion; Cambridge University, Scott Polar Research

	Institute
Keywords:	Glacier hydrology, Subglacial sediments, Subglacial processes, Glacial tills, Ice dynamics
Abstract:	<p>Subglacial hydrology modulates basal motion but remains poorly constrained, particularly for soft-bedded Greenlandic outlet glaciers. Here, we report detailed measurements of the response of subglacial water pressure to the connection and drainage of adjacent water-filled boreholes drilled through kilometre-thick ice on Sermeq Kujalleq (Store Glacier). These measurements provide evidence for elastic gap opening at the ice-sediment interface, Darcian flow through the sediment layer, and the forcing of water pressure in hydraulically-isolated cavities by elastic stress transfer. We observed a small pressure drop followed by a large pressure rise in response to the connection of an adjacent borehole, consistent with the propagation of a flexural wave within the ice and underlying deformable sediment. We interpret the delayed pressure rise as evidence of no pre-existing conduit and the progressive decrease in hydraulic transmissivity as the closure of a narrow < 1.5 mm gap opened at the ice-sediment interface, and a reversion to Darcian flow through the sediment layer with a hydraulic conductivity of $\leq 10^{-6}$ m s$^{-1}$. We suggest that gap opening at the ice-sediment interface deserves further attention as it will occur naturally in response to the rapid pressurisation of water at the bed.</p>

SCHOLARONE™
Manuscripts

1 **Water flow through sediments and at the ice-sediment**
2 **interface beneath Sermeq Kujalleq (Store Glacier),**
3 **Greenland**

4 Samuel H. Doyle,¹ Bryn Hubbard,¹ Poul Christoffersen,² Robert Law,²
5 Duncan R. Hewitt,³ Jerome A. Neufeld,^{4,5,6} Charlotte M. Schoonman,^{2*}
6 Thomas R. Chudley,^{2†} Marion Bougamont²

7 ¹*Centre for Glaciology, Department of Geography and Earth Sciences, Aberystwyth University,*
8 *Aberystwyth, SY23 3DB, UK*

9 ²*Scott Polar Research Institute, Cambridge University, Cambridge, CB2 1ER, UK*

10 ³*Department of Mathematics, University College London, 25 Gordon Street, London, WC1H 0AY*

11 ⁴*Institute of Theoretical Geophysics, Department of Applied Mathematics and Theoretical Physics,*
12 *University of Cambridge, Wilberforce Road, Cambridge CB3 0WA, UK*

13 ⁵*BP Institute, University of Cambridge, Madingley Rise, Cambridge CB3 0EZ, UK*

14 ⁶*Department of Earth Sciences, Bullard Laboratories, University of Cambridge, Madingley Rise,*
15 *Cambridge CB3 0EZ, UK*

16 *Correspondence: Samuel Doyle (sdd08@aber.ac.uk)*

17 **ABSTRACT.** Subglacial hydrology modulates basal motion but remains
18 **poorly constrained, particularly for soft-bedded Greenlandic outlet glaciers.**
19 **Here, we report detailed measurements of the response of subglacial water**
20 **pressure to the connection and drainage of adjacent water-filled boreholes**
21 **drilled through kilometre-thick ice on Sermeq Kujalleq (Store Glacier).**
22 **These measurements provide evidence for elastic gap opening at the ice-**
23 **sediment interface, Darcian flow through the sediment layer, and the forcing of**
24 **water pressure in hydraulically-isolated cavities by elastic stress transfer. We**

25 observed a small pressure drop followed by a large pressure rise in response
 26 to the connection of an adjacent borehole, consistent with the propagation
 27 of a flexural wave within the ice and underlying deformable sediment. We
 28 interpret the delayed pressure rise as evidence of no pre-existing conduit and
 29 the progressive decrease in hydraulic transmissivity as the closure of a narrow
 30 (< 1.5 mm) gap opened at the ice-sediment interface, and a reversion to Darcian
 31 flow through the sediment layer with a hydraulic conductivity of $\leq 10^{-6}$ m s $^{-1}$.
 32 We suggest that gap opening at the ice-sediment interface deserves further
 33 attention as it will occur naturally in response to the rapid pressurisation of
 34 water at the bed.

35 LIST OF SYMBOLS

36	α	Surface and bed slope ($^{\circ}$)
37	β_w	Water compressibility (5.1×10^{-10} Pa $^{-1}$)
38	b	Sediment thickness (m)
39	B	Bending modulus of the ice (Pa m 3)
40	δ	Gap width (m)
41	D	Time constant (s)
42	ϕ	Areal fraction of the bed covered by gap
43	f_D	Frictional drag coefficient
44	F	Force on the drill tower (N)
45	γ	Clausius-Clapeyron constant (9.14×10^{-8} K Pa $^{-1}$)
46	g	Gravitational acceleration (9.81 m s $^{-2}$)
47	h	Hydraulic head (m)
48	h_0	Reference hydraulic head (m)
49	H_i	Ice thickness (m)
50	H_w	Water height (m)

*Present address: Alfred Wegener Institute, Helmholtz Centre for Polar and Marine Research, Bremerhaven, Germany

†Present address: School of Natural and Environmental Sciences, Newcastle University, Newcastle Upon Tyne, NE1 7RU, UK

51	K	Hydraulic conductivity (m s^{-1})
52	M	Sediment stiffness (p-wave modulus) (Pa)
53	N	Effective pressure (Pa)
54	p_i	Ice overburden pressure (Pa)
55	p_w	Subglacial water pressure (Pa)
56	p_{tr}	Triple point pressure of water (611.73 Pa)
57	Q	Volumetric flux ($\text{m}^3 \text{s}^{-1}$)
58	ρ_i	Ice density ($910 \pm 10 \text{ kg m}^{-3}$)
59	ρ_w	Water density at 0°C (999.8 kg m^{-3})
60	ρ_d	Hose density (kg m^{-3})
61	r	Radial distance (m)
62	r_d	External hose radius (0.015 m)
63	r_0	Borehole radius at base (m)
64	r_s	Borehole radius at near-surface (m)
65	R	Radius of influence (m)
66	Re	Reynolds number
67	s	Recharge ($s = h - h_0$) (m)
68	s_0	Reference recharge (m)
69	S	Storage coefficient (m)
70	t	Time (s)
71	T	Hydraulic transmissivity ($\text{m}^2 \text{s}^{-1}$)
72	T_m	Melting temperature of ice ($^\circ\text{C}$)
73	T_{tr}	Triple point temperature of water (273.16 K)
74	μ_w	Water viscosity at 0°C (0.0018 Pa.s)
75	U_d	Drill velocity (m min^{-1})
76	U_w	Water velocity (m s^{-1})
77	V	Volume (m^3)
78	$W(u)$	
79		Well function
80	z	Orthometric height (m)

81 1. INTRODUCTION

82 The nature of subglacial hydrology and basal motion on ice masses underlain by soft sediments are central
83 questions in ice dynamics (e.g. Tulaczyk and others, 2000; Clarke, 1987; Murray, 1997). However, despite
84 abundant evidence for subglacial sediments beneath fast-moving outlet glaciers and ice streams draining the
85 Greenland and Antarctic ice sheets (e.g. Alley and others, 1986; Blankenship and others, 1986; Christianson
86 and others, 2014) and mountain glaciers (e.g. Humphrey and others, 1993; Iverson and others, 1995) soft-
87 bedded processes remain poorly constrained (Alley and others, 2019; Walter and others, 2014). Water
88 flow in a soft-bedded subglacial environment has been hypothesised to occur via: Darcian flow through
89 permeable sediments (Clarke, 1987); sheet flow at the ice-sediment interface (e.g. Weertman, 1970; Alley
90 and others, 1989; Flowers and Clarke, 2002; Creyts and Schoof, 2009); and concentrated flow in channels
91 cut into the ice and canals eroded into the sediment (Walder and Fowler, 1994; Ng, 2000). Drainage through
92 gaps opened and closed dynamically at the ice-sediment interface by turbulent water flow at high pressure
93 has also been proposed as an explanation for the rapid drainage of boreholes (Engelhardt and Kamb, 1997;
94 Kamb, 2001) and both supra- and pro-glacial lakes (Sugiyama and others, 2008; Tsai and Rice, 2010, 2012;
95 Hewitt and others, 2018). Direct evidence for gap-opening at the ice-sediment interface is limited to two
96 observational studies (Engelhardt and Kamb, 1997; Lüthi, 1999). However, despite support from detailed
97 analytical modelling (Schoof and others, 2012; Rada and Schoof, 2018) dynamic gap opening has yet to be
98 fully developed for larger-scale numerical models of subglacial hydrology.

99 The water-saturated sediment layer beneath a soft-bedded ice mass can be approximated as an aquifer
100 confined by an overlying ice aquiclude (e.g. Lingle and Brown, 1987; Stone and Clarke, 1993). And,
101 with careful adaptation, standard hydrogeological techniques can be used to estimate subglacial aquifer
102 properties such as transmissivity, conductivity, diffusivity, and storativity. These include slug tests, where
103 the borehole water level is perturbed by the insertion and sudden removal of a sealed pipe of known
104 volume (Stone and Clarke, 1993; Stone and others, 1997; Iken and others, 1996; Kulesa and Hubbard,
105 1997; Kulesa and Murray, 2003; Kulesa and others, 2005; Hodge, 1979), packer tests where the borehole
106 is sealed near the surface and subsequently rapidly pressurised with air (Stone and Clarke, 1993; Stone
107 and others, 1997), and pumping tests where the borehole hydraulic head is monitored in response to water
108 injection or extraction (e.g. Engelhardt, 1978; Engelhardt and Kamb, 1997; Iken and Bindenschadler, 1986;
109 Lüthi, 1999). Borehole drainage on connection with the bed (hereafter 'breakthrough'), and the recovery to
110 equilibrium water levels have also been used to determine subglacial aquifer properties (e.g. Engelhardt and

111 Kamb, 1997; Stone and Clarke, 1993; Stone and others, 1997; Lüthi, 1999). During breakthrough events the
112 water level in the initially water-full borehole either: (i) drops rapidly to a new equilibrium level some tens
113 of metres below the surface, (ii) does not drop at all, or (iii) drops slowly, or rapidly, to a new equilibrium
114 level after a delay of minutes to days, with the variability in response usually explained in terms of the
115 connectivity of the subglacial drainage system (e.g. Smart, 1996; Gordon and others, 2001). The hydraulic
116 conductivity of a subglacial sediment layer has also been derived from the propagation and attenuation of
117 diurnal subglacial water pressure waves (e.g. Hubbard and others, 1995), and from numerical modelling of
118 the pressure peaks induced when pressure sensors freeze in (Waddington and Clarke, 1995). To date, the
119 application of borehole response tests to marine-terminating glaciers in Greenland is limited to a single
120 study (Lüthi, 1999), presumably due to the challenges of adapting groundwater techniques to the ice sheet
121 setting.

122 The application of hydrogeological techniques requires a number of simplifying assumptions. Many
123 techniques are fundamentally based on Darcian flow and inherently assume that the aquifer is isotropic and
124 homogeneous; conditions that may rarely be met in the subglacial environment. Water flow in groundwater
125 investigations is typically slow and assumed to be Darcian. While this may hold for low-velocity water flow
126 through subglacial sediments, the discharge rates during borehole breakthrough events mean turbulent flow
127 is likely in the vicinity of the borehole base (e.g. Stone and Clarke, 1993). Further complications arise due
128 to the greater density of water than ice, overpressurising the ice at the base of water-filled glacier boreholes
129 with the potential to raise the ice from its substrate permitting water to flow through the gap created.
130 (Overpressure here being water pressure in excess of the ice overburden pressure). Previous studies have
131 attempted to determine the widths of such gaps (Weertman, 1970; Engelhardt and Kamb, 1997; Lüthi,
132 1999).

133 Ice boreholes provide direct access to the subglacial environment allowing sensor installation and borehole
134 response tests. Here, we analyse borehole response tests conducted on Sermeq Kujalleq (Store Glacier) in
135 West Greenland during summer 2019. The response tests included breakthrough events, which occurred
136 consistently when boreholes intersected the ice-sediment interface, constant-rate pumping tests undertaken
137 as water is pumped into the borehole as the drill stem was raised to the surface, and recovery tests
138 following removal of the stem. The results provide insights into subglacial hydrological conditions and
139 permit estimation of the hydraulic transmissivity and conductivity of the subglacial drainage system.

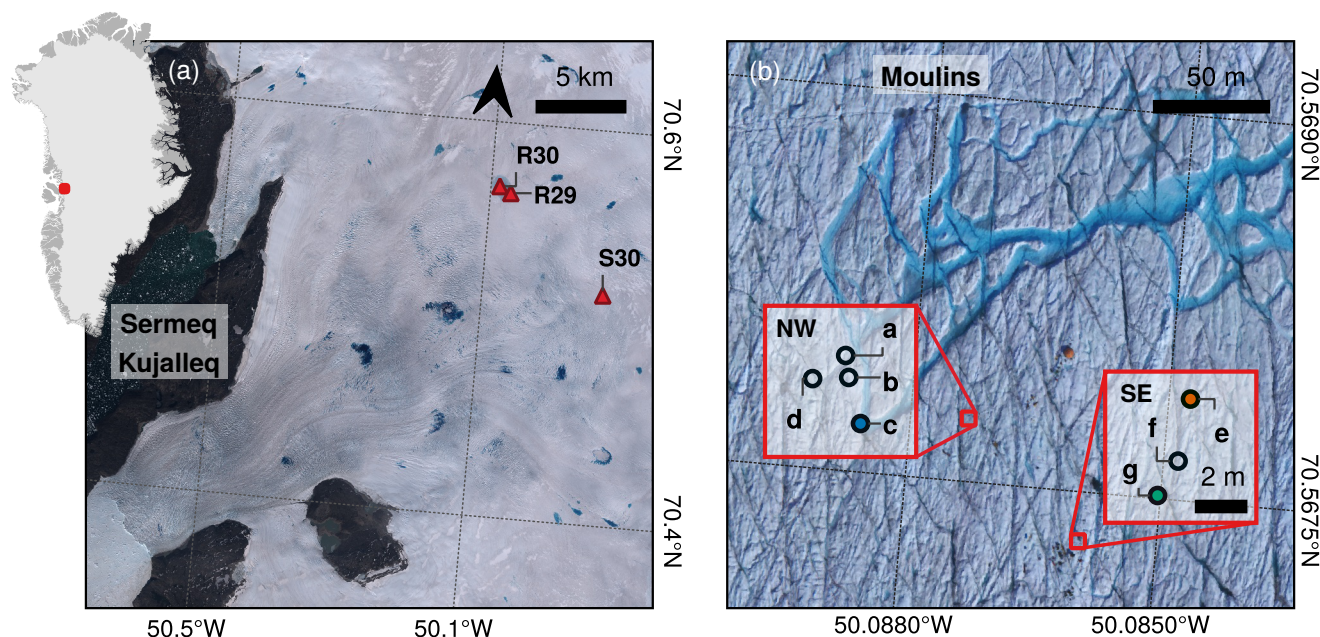


Fig. 1. Maps of the field site. (a) Location of the study site R30 on Sermeq Kujalleq (Store Glacier) with the location of the R29 and S30 drill sites also marked. The background is a Sentinel-2 image acquired on 1 June 2019 and the red square on the inset map shows the location in Greenland. (b) Close up of the R30 study site showing the location of boreholes and moulins. Three boreholes intersected the ice-sediment interface (filled, colour-coded circles) and four terminated above the base (hollow circles). The background orthophoto was acquired by an uncrewed aerial vehicle survey following Chudley and others (2019a) on 21 July 2019.

140 2. METHODS

141 2.1. Field site

142 Sermeq Kujalleq (Store Glacier) is a major fast-moving outlet glacier of the Greenland Ice Sheet draining an
 143 $\sim 34,000 \text{ km}^2$ catchment area (Rignot and others, 2008) into Ikerasak Fjord — a tributary of Uummannaq
 144 Fjord. In summer 2019, we used pressurised hot water to drill seven boreholes on Sermeq Kujalleq (Store
 145 Glacier) at site R30 ($N70^\circ 34.0'$, $W050^\circ 5.2'$) located in the centre of the drained bed of supraglacial lake
 146 L028 (Fig. 1a; Table S1). R30 lies 30 km from the calving front at 863 masl and is within the ablation
 147 area; there was no winter snow or firn present during the drilling campaign. Ice flow measured by a
 148 Global Navigation Satellite System (GNSS) receiver averaged 521 m yr^{-1} in the SSW direction (217° True)
 149 between 9 July and 16 September 2019. The surface slope was calculated as 1.0° from linear regression of the
 150 ArcticDEM digital elevation model (Porter and others, 2018) over a distance of ten ice thicknesses (10 km).
 151 Lake L028 drained via hydraulic fracture on 31 May 2019 (Chudley and others, 2019b) forming two major
 152 moulins (each of diameter $\sim 6 \text{ m}$) located within 200 m of the drill site (Fig. 1b). Borehole-based Distributed

153 Acoustic Sensing (DAS) in BH19c provides evidence for up to 37 m of consolidated subglacial sediment at
154 R30 (Booth and others, 2020), while seismic reflection surveys at site S30 (8 km to the south-east of R30;
155 Fig. 1a) revealed up to 45 m of unconsolidated sediment overlying consolidated sediment (Hofstede and
156 others, 2018). Borehole-based investigations of englacial and basal conditions at S30 reported low effective
157 pressures (180 – 280 kPa), an absent or thin (< 10 m) basal temperate ice layer, and internal deformation
158 concentrated within the lowermost 100 m of ice, below the transition between interglacial (Holocene) and
159 last-glacial (Wisconsin) ice (LGIT; Doyle and others, 2018; Young and others, 2019). At R30, Distributed
160 Temperature Sensing (DTS) reveals a 70-m-thick basal temperate ice layer, the LGIT at 889 m depth, and
161 a steeply curving temperature profile with a minimum ice temperature of -20.8°C near the centre of the
162 ice column (Law and others, 2021).

163 2.2. Hot water drilling

164 Boreholes were drilled using the hot water drill system described in Doyle and others (2018). Pressurised, hot
165 water (1.1 MPa; $\sim 80^{\circ}\text{C}$) was provided by five pressure-heater units (Kärcher HDS1000DE) at a regulated
166 flow rate of 75 l min^{-1} , through a 1,350 m long, 19.3 mm (0.75") bore hose. A load cell and rotary encoder
167 recorded the load on the drill tower and the hose length below the surface at 0.5 Hz with a resolution of
168 1 kg and 0.1 m respectively (Figs. S1-S3). Borehole logging to a depth of 325 m indicates that the hot water
169 drilling system consistently drills boreholes that are within 1° of vertical (Hubbard and others, 2021).

170 Boreholes (BH) were named by year and by letter in chronological order of drilling, with BH19a the first
171 borehole drilled in 2019 (Table S1). Boreholes were drilled in two clusters with the first (BH19a, b, c, and
172 d) separated from the second (BH19e, f, and g) by 70 m (Fig. 1b). Seven boreholes were drilled in 2019
173 with three reaching the ice-sediment interface at depths of 1043 m (BH19c), 1022 m (BH19e), and 1039 m
174 (BH19g), giving a mean ice thickness of 1035 m and mean elevation of the glacier sole of -172 m asl (Table
175 1). Four boreholes were terminated above the ice-sediment interface (see Table S1). Prior to breakthrough
176 boreholes were water-filled to the bare ice surface, with excess water supplied by the pressure-heater units
177 overflowing from the top of the borehole.

178 To reduce overall drilling duration and produce a more uniform borehole radius (0.06 m four hours after
179 termination of drilling), we optimised drilling speed using the numerical borehole model of Greenler and
180 others (2014). The borehole model was constrained by ice temperature from BH18b at site R29, 1.1 km
181 distant (Fig. 1a; Hubbard and others, 2021), and a hose thermal conductivity of $0.24\text{ W m}^{-1}\text{ K}^{-1}$. Borehole
182 radius at the point of breakthrough was then estimated by re-running the model with the recorded drill

183 speeds and the equilibrated ice temperature profile measured in BH19c at site R30 (Law and others, 2021).
184 The mean borehole radius for BH19c, BH19e and BH19g output by the model at the time of borehole
185 breakthrough was 0.07 m, with larger radii (mean of 0.10 m) in the lowermost 100 m of the ice column
186 (Table B1) due to intentionally slower drilling as the drill approached the ice-sediment interface, together
187 with the presence of temperate ice that was unaccounted for during initial model runs. The borehole
188 model underestimated the near-surface (i.e. 0 – 100 m) borehole radius (r_s), possibly due to turbulent heat
189 exchange that is not included in the model, so we use the radius at the water line calculated for BH19g
190 (0.14 m) as r_s for all the borehole response tests (see Appendix B).

191 Analysis of the temperature time series recorded by DTS in BH19c (Law and others, 2021) shows that
192 the boreholes rapidly froze shut. At 580 m depth, where the undisturbed ice temperature was -21.1°C , the
193 temperature fell below the pressure-dependent melting temperature 3 h after drilling. Within warmer ice
194 refreezing was slower: at 920 m depth in BH19c the ice temperature was -3°C and refreezing was complete
195 after 5 days.

196 2.3. Pressure measurements

197 Basal water pressures were recorded by vibrating wire piezometers (Geokon 4500SH) installed at the base
198 of BH19c and BH19e and a current loop transducer (Omega Engineering Ltd. PXM319) installed at the
199 base of BH19g. Pressure records from the Geokon 4500SH were zeroed with atmospheric pressure at the
200 surface, temperature compensated using a high-accuracy thermistor in contact with the piezometer body,
201 and calibrated using the manufacturer's second-order polynomial to an accuracy of ± 3 kPa, equivalent
202 to ± 0.3 m of hydraulic head. The pressure record from the PXM319 current loop transducer (accuracy
203 = ± 35 kPa, equivalent to ± 3.6 m of head) was calibrated using the manufacturer's linear calibration and
204 zeroed with atmospheric pressure at the surface. A pressure spike indicates that the ice surrounding the
205 transducer installed in BH19g froze at 13.7 h post-breakthrough.

All pressure sensors were lowered until contact with the ice-bed interface was confirmed by the pressure ceasing to increase. The sensor was then raised slightly (piezometer offset: 0.05 – 0.4 m; Table 1) to prevent the piezometer from being dragged through the substrate. The borehole water level below the surface (that is the length of the uppermost air-filled section of the borehole) at installation was measured with a well depth meter, and by reference to distance markers on the piezometer cable. The final installation depth was determined by adding this water level to the depth recorded by the piezometer. The ice thickness (H_i) was calculated by adding the piezometer offset to the final installation depth. Borehole positions

were surveyed on 22 July 2019 using a Trimble R9s GNSS receiver with 8 min long observations post-processed using the precise point positioning service provided by Natural Resources Canada (CSRS-PPP). Borehole surface elevation was converted to orthometric EGM96 geoid heights. To allow inter-comparison of pressure records from sensors installed at different depths below the surface, water pressure was expressed as hydraulic head h , which represents the theoretical orthometric height of the borehole water level,

$$h = \frac{p_w}{\rho_w g} + z, \quad (1)$$

where $\rho_w = 999.8 \text{ kg m}^{-3}$ is water density at 0°C , $g = 9.81 \text{ m s}^{-2}$ is gravitational acceleration and z is the orthometric height of the piezometer determined by subtracting the piezometer depth below the surface from the orthometric height of the borehole at the surface. Pressure was also expressed as the effective pressure $N = p_i - p_w$ and the overpressure ($p_w - p_i$), the latter in respect of the excess pressure exerted at the base of water-filled boreholes due to the greater density of water than ice (Table 1). The ice-overburden pressure p_i was approximated for an inclined, parallel-sided slab of ice as

$$p_i = \rho_i g H_i \cos \alpha, \quad (2)$$

206 where ρ_i is the density of ice, H_i is the height of the overlying ice column, and $\alpha = 1.0^\circ$ is the mean surface
207 and bed slope (see Section 2.1), and ice density was taken as $\rho_i = 910 \pm 10 \text{ kg m}^{-3}$.

208 2.4. Temperature measurements

Temperature was measured using high-accuracy ($\pm 0.05^\circ\text{C}$) thermistors (Littelfuse: PR502J2) at $\sim 0, 1, 3, 5,$ and 10 m above the bed in BH19c and BH19e and also throughout the full ice column in BH19c using fibre-optic DTS (Law and others, 2021). Here we present temperature measurements recorded by the lowermost thermistor in BH19c, which was mounted with the Geokon 4500SH piezometer. We calculated the pressure-dependent melting temperature

$$T_m = T_{tr} - \gamma(p_i - p_{tr}), \quad (3)$$

209 where $\gamma = 9.14 \times 10^{-8} \text{ K Pa}^{-1}$ is the Clausius-Clapeyron gradient determined from the basal temperature
210 gradient (Law and others, 2021), and $T_{tr} = 273.16 \text{ K}$ and $p_{tr} = 611.73 \text{ Pa}$ are the triple point temperature
211 and pressure of water respectively.

Table 1. Key data for the boreholes that reached the bed. Variables h_0 , p_w , and N were calculated for the reference period 36-60 h after each respective breakthrough, which was deemed representative of subglacial water pressure.

	BH19c	BH19e	BH19g	Mean
Ice thickness (m)	1043.0	1022.3	1039.2	1034.8
Piezometer offset (m)	0.05	0.1	0.4	0.18
Piezometer orthometric height (m asl)	-180.5	-159.6	-175.1	-171.7
Water-full overpressure (kPa)	921 ± 102	902 ± 100	917 ± 102	913 ± 101
Breakthrough time (UTC)	5 July 2019 02:54:36	12 July 2019 03:39:35	22 July 2019 08:07:23	n/a
Breakthrough volume (m ³)	4.83	4.50	4.93	4.75
Peak load (kg)	199	180	214	198
Drill-indicated breakthrough depth* (m)	1031.0	1010.5	1017.3	1019.6
Drill-indicated maximum depth* (m)	1031.0	1013.3	1017.4	1020.6
Pump rate (l min ⁻¹)	75	75	75	75
Pumping duration during raise (min)	140	140	118	133
Volume of water pumped during raise (m ³)	10.5	10.5	8.9	10.0
Recovery time (h)	36.4	49.7	45.4	43.8
Initial water level depth (m)	78.1	72.9	79.8	76.9
h_0 (m)	773.0	777.1	775.9 [†]	775.3
p_i (MPa)	9.310 ± 0.1	9.125 ± 0.1	9.276 ± 0.1	9.237 ± 0.1
p_w (MPa)	9.352	9.178	9.166 [†]	9.232
p_w (% of p_i)	100.5 ± 1.1	100.6 ± 1.1	100.5 ± 1.1 [†]	100.5 ± 1.1
N (kPa)	-43 ± 102	-54 ± 102	-42 ± 102 [†]	-46 ± 102

*Drill-indicated depths do not account for the elastic extension of the hose under load.

[†]Recorded in BH19e due to freeze-in of pressure transducer in BH19g.

212 2.5. GNSS Measurements of ice motion

213 Time series of horizontal and vertical ice motion were determined from dual frequency (L1 + L2) GNSS
 214 data recorded by a Trimble R7 receiver at 0.1 Hz and post-processed kinematically using the CSRS-PPP
 215 service. The GNSS antenna was mounted on a 5 m long pole drilled 4 m into the ice surface. Rapid re-
 216 freezing of the hole ensured effective coupling of the antenna pole with the ice. Small gaps (< 5 min) in the
 217 position record were interpolated linearly before a 12 h moving average was applied. The filtered position
 218 record was differentiated to calculate velocity. The time series was then resampled to 10 min medians and a

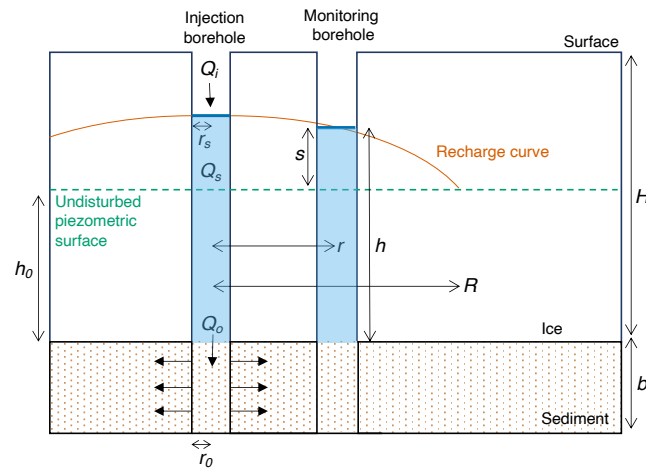


Fig. 2. Conceptual diagram and nomenclature for borehole drainage via radial Darcian flow through a subglacial sediment aquifer confined by an overlying ice aquiclude. Note that monitoring boreholes are likely to have refrozen at the time of the tests and h is therefore the equivalent hydraulic head for the subglacial water pressure recorded.

219 further 3 h moving average was applied to the velocity record. To prevent a shift in phase, centred moving
 220 averages and centred differences were used.

221 3. BOREHOLE RESPONSE TESTS

222 We analysed the response of borehole water pressure to the perturbations induced at breakthrough,
 223 during the continued pumping of water into the borehole while the drill stem and hose were raised to
 224 the surface, and also during the recovery phase after which borehole water pressure was in equilibrium
 225 with the pressure in the subglacial drainage system. These tests were conducted at different times since
 226 breakthrough, allowing us to investigate whether hydraulic transmissivity changed as water pressure
 227 returned to equilibrium. Rapid borehole refreezing precluded slug testing. Below we describe the borehole
 228 response test results alongside the methods.

229 For the majority of tests the monitoring borehole was the same as the injection borehole and these are
 230 referred to simply by the borehole name. To distinguish response tests where the injection and monitoring
 231 boreholes were different we give the injection borehole in full followed by the monitoring borehole's letter
 232 code in brackets. A conceptual illustration of our borehole response tests is presented in Figure 2.

233 All data loggers, including that of the drill, were synchronised precisely with Global Positioning System
 234 Time (GPST) immediately prior to drilling. Water pressure data were logged by separate Campbell
 235 Scientific CR1000X data loggers for each cluster of boreholes. The sampling frequency was increased to

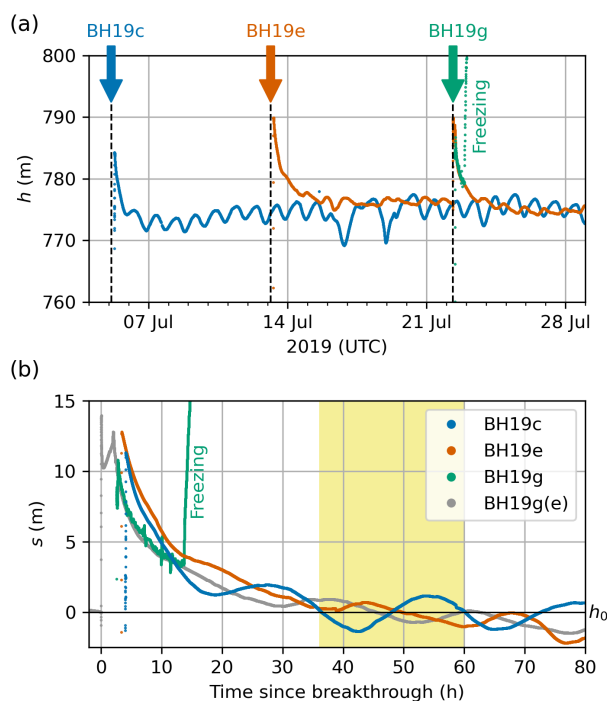


Fig. 3. (a) Time series of hydraulic head (h). Borehole breakthrough times are marked with a vertical dashed line and arrow. (b) Time series of head above the reference head ($s = h - h_0$) plotted against time since respective breakthrough for all breakthrough tests. The yellow shade marks the 24 h period selected to define h_0 (36 – 60 h post-breakthrough).

236 0.2 Hz prior to borehole breakthrough, necessitating temporary suspension of thermistor measurements.
 237 Hence, no measurements of basal water temperature were made when drilling was taking place.

238 As it is difficult to measure the background hydraulic head without disturbing the subglacial environment
 239 it is necessary to define a reference head (h_0). The mean head in BH19e 36 – 60 h after BH19g breakthrough
 240 had recovered to within 0.1 m of the mean head over the 24 h period preceding BH19g breakthrough (Fig.
 241 3b). On this basis, we define h_0 as the mean head from 36 – 60 h post-breakthrough for all tests. No
 242 corrections for background trends in hydraulic head were made but such trends are small relative to the
 243 perturbations induced (Fig. 3a).

244 3.1. Breakthrough tests

245 3.1.1. Observations

246 All three boreholes drilled to the bed in 2019 drained rapidly upon intersecting the basal interface. During
 247 breakthrough, water levels dropped to an initial level measured during pressure transducer installation of
 248 78, 73, and 80 m below the surface in BH19c, BH19e and BH19g (Table 1). The frictional drag of water

249 flowing past the hose during breakthrough events caused transient ~ 2 kN magnitude peak forces as recorded
 250 on the drill tower (Figs. 4, S1-S3). Following the peak, force on the drill tower became constant at ~ 200 s
 251 post-breakthrough but at a higher level than recorded prior to breakthrough. The offset in the pre- and
 252 post-breakthrough force on the drill tower represents the difference between the weight of the hose in a
 253 water-filled and part-filled borehole.

As the drill stem was raised to the surface over ~ 2 h water continued to be pumped into the borehole, supplying an additional ~ 10 m³ of water (Table 1). The volume of water drained during the breakthrough events was determined from the initial water level and annular cross-sectional area of the borehole of near surface radius (r_s) containing the hose of external radius (r_d), yielding a mean volume for the three breakthrough events of 4.70 m³ (Table 1). Taking the duration of rapid drainage as the duration of the peak in force of ~ 200 s gives a mean discharge for the three breakthrough events of 2.3×10^{-2} m³ s⁻¹ supplied from the borehole, with an additional flux supplied by the pumps $Q_i = 75$ l min⁻¹ (1.25×10^{-3} m³ s⁻¹) bringing the total discharge to $Q_o = 2.5 \times 10^{-2}$ m³ s⁻¹ and the total volume over the ~ 200 s duration to 4.95 m³. The Reynolds number for outflow from the base of the borehole can be approximated as flow through a uniform cylindrical pipe, with a radius equal to that at the borehole base, the mean of which was $r_0 = 0.10$ m for the three boreholes (Table B1),

$$Re = \frac{U_w 2r_0 \rho_w}{\mu_w} = \frac{2Q_o \rho_w}{\pi \mu_w r_0}, \quad (4)$$

254 where $\mu_w = 0.0018$ Pa s is the water viscosity at 0°C. Water flow through the boreholes near the base was
 255 turbulent with a high $Re \approx 87,500$ greatly exceeding the threshold for laminar flow of 2,000 (de Marsily,
 256 1986).

257 3.1.2. Determining the BH19g breakthrough flux

258 To avoid sensor cables becoming tangled around the drill hose, pressure transducers were installed after the
 259 drill stem and hose had been recovered to the surface. Hence, no measurements of pressure were made within
 260 boreholes being drilled including during breakthrough. As the pressure response to BH19g breakthrough
 261 was captured by transducers already installed in BH19c and BH19e (Fig. 4) we now focus on the BH19g
 262 breakthrough.

We determined the time varying flux of water into the subglacial drainage system during the breakthrough of BH19g by inverting the recorded force on the drill tower from the hose, which is a combination of its weight, both in air and in water, and the frictional drag on the hose when the water drains through the

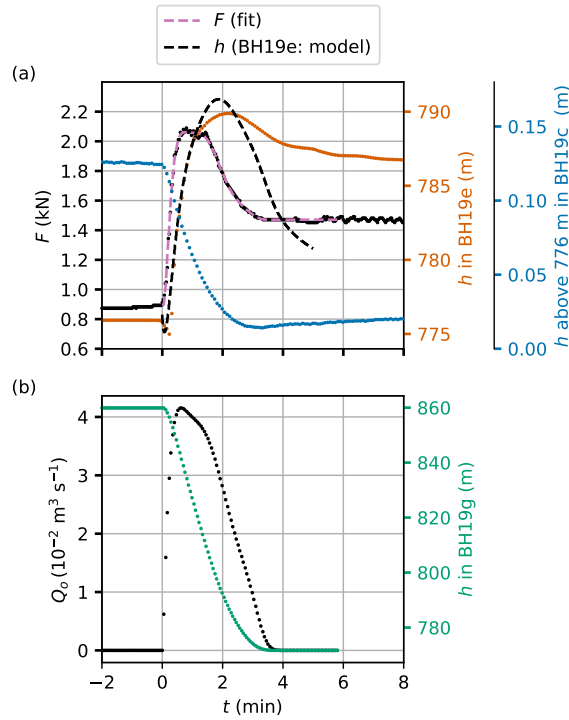


Fig. 4. (a) Force on the drill tower with best fit plotted against time since BH19g breakthrough, together with measured and modelled hydraulic head. (b) Volumetric flux into the subglacial drainage system (Q_o) and hydraulic head in BH19g determined by inverting the force on the drill tower.

borehole,

$$F(t) = \pi r_d^2 \bar{\rho}_d g (H_{w0} - H_w) + \pi r_d^2 \Delta \bar{\rho} g H_w + \frac{\pi r_d}{4} f_D \rho_w U_w^2 H_w + F_{ds}, \quad (5)$$

263 where r_d is the radius of the drill, $\bar{\rho}_d$ is the mean density of the drill (including the water core), $\Delta \bar{\rho} = \bar{\rho}_d - \rho_w$,
 264 f_D is the coefficient of frictional drag exerted on the outside of the hose by the down-rushing water in the
 265 borehole, $H_w(t)$ is the height of water in the borehole, F_{ds} is the force exerted by the weight of the drill
 266 stem in water, and the velocity of water in the borehole during the drainage event is $U_w(t) = dH_w/dt$.

The force on the drill hose is initially set by the water height, which for a borehole full to the surface is equal to the ice thickness, therefore $H_w(t=0) = H_{w0} = H_i = 1039$ m (Table 1). Since the initial force just before breakthrough $F_0 = 893$ N the density difference between the hose and water is

$$\Delta \bar{\rho} = \frac{F_0 - F_{ds}}{\pi r_d^2 g H_{w0}} = 96 \text{ kg m}^{-3}. \quad (6)$$

Taking $\rho_w = 999.8 \text{ kg m}^{-3}$ gives a mean density of the hose filled with water $\bar{\rho}_d = 1096 \text{ kg m}^{-3}$. Note that the composite density of the hose is

$$\bar{\rho}_d = \rho_d - (\rho_d - \rho_w)(r_d/\underline{r}_d)^2, \quad (7)$$

267 where ρ_d is the density of the hose material, and $\underline{r}_d = 9.7 \text{ mm}$ is the internal bore radius of the hose. Using
 268 the calculated value of $\bar{\rho}_d = 1096 \text{ kg m}^{-3}$ gives an estimate of the hose material density of $\rho_d = 1166 \text{ kg m}^{-3}$,
 269 which is slightly larger than the nominal manufacturer's specification of 1149 kg m^{-3} . This apparent extra
 270 density corresponds to an extra force measured on the drill tower prior to breakthrough of 65 N , which we
 271 interpret as a drag of 0.0625 N per metre of hose from the pumped water flowing down the centre of the
 272 hose.

Neglecting minor residual oscillations, the force $F_\infty = F(t \rightarrow \infty)$ on the drill tower after the initial rapid breakthrough was again approximately constant and is given by

$$F_\infty = 1470 \pm 10 \text{ N} = \pi r_d^2 g [\bar{\rho}_d (H_{w0} - H_{w\infty}) + \Delta \bar{\rho} H_\infty]. \quad (8)$$

273 From this we can infer that the final height of the water level $H_{w\infty} = 954 \pm 1 \text{ m}$. That is, during BH19g
 274 breakthrough the water in BH19g transiently drops $H_{w0} - H_{w\infty} \approx 85 \text{ m}$ below the surface.

Following BH19g breakthrough a portion of the water in the borehole is rapidly evacuated into the subglacial environment. We know that the water level in the borehole decreases monotonically from an initial height H_0 to a final height H_∞ and so fit the transient response with a modified exponential solution of the form

$$H_w = H_{w\infty} + (H_{w0} - H_{w\infty})e^{-y(t)}, \quad (9)$$

where

$$y(t) = c_1 t + c_2 t^2 + c_3 t^3 + c_4 t^4 + c_5 t^5 + c_6 t^6. \quad (10)$$

A sixth order polynomial was found to be the lowest order of polynomial to accurately represent the data.

The flux of water from the borehole into the subglacial environment (Q_o) can then be given by

$$\begin{aligned} Q_o(t) &= \pi r_d^2 U_w(t) + Q_i = \pi r_d^2 \frac{dH_w}{dt} + Q_i, \\ &= -\pi r_d^2 \frac{dp_w}{dt} e^{-y(t)} + Q_i, \end{aligned} \quad (11)$$

275 where $Q_i = 1.25 \times 10^{-3} \text{ m s}^{-3}$ is the input flux from the drill. The six constants in the polynomial $y(t)$,
 276 c_i where $i = 1, \dots, 6$, along with the drag coefficient f_D were estimated using nonlinear regression. The

277 resulting constants, with error estimation, are given in Table S2. From this fit ($R^2 = 0.996$) of the force
 278 on the drill hose the height of water in the borehole can be calculated together with the flux into the
 279 subglacial hydrological network (Fig. 4b). This reveals that the discharge peaked at $4.2 \times 10^{-2} \text{ m}^3 \text{ s}^{-1}$ 38 s
 280 after breakthrough.

281 3.1.3. Modelling the pressure response to BH19g breakthrough

282 Distinct pressure perturbations occurred in BH19c and BH19e following the breakthrough of BH19g (Fig.
 283 4a). In BH19e, located 4.1 m from BH19g, pressure instantaneously decreased by 0.93 m over a 20 ± 5 s period
 284 before rising rapidly and peaking at 14.0 m above its pre-breakthrough level 130 ± 5 s post-breakthrough.
 285 Synchronously with the pressure drop observed in BH19e, a 0.11 m drop in hydraulic head began in BH19c.

286 To analyse these pressure perturbations further we modelled the propagation of water at the contact
 287 between elastic ice and poroelastic sediment during BH19g breakthrough following Hewitt and others
 288 (2018). This model accounts for pressure diffusion, flexure of the ice, and deformation of the sediment, and
 289 was originally developed to describe the subglacial response to a rapidly draining supraglacial lake. The
 290 original model, which is based on Darcy's law, allowed for the formation of a subglacial cavity as well as
 291 seepage through the sediment or established subglacial networks. However, for simplicity, here we do not
 292 include cavity formation and instead assume a single effective hydraulic transmissivity for subglacial water
 293 transport; and that the fluid is incompressible. The model allows the poroelastic sediment layer to deform
 294 in response to fluid flow and pressure gradients, which allows the overlying ice to flex and bend slightly
 295 as reflected in the small (0.93 m) transient pressure decrease preceding the large (14.0 m) pressure increase
 296 recorded in BH19e following BH19g breakthrough (Fig. 4a). With these features included, the model shows
 297 how an injected fluid diffuses through the subglacial environment and how this drives a propagating flexural
 298 wave in the overlying ice.

The linearised form of the model reduces to an evolution equation for the subglacial water pressure,
 which for consistency is here expressed as hydraulic head h

$$\rho g \frac{\partial h}{\partial t} = A_1 \nabla^2 h + A_2 \nabla^6 h. \quad (12)$$

Here $A_1 = TM/b$ and $A_2 = TB$, in terms of transmissivity T , till stiffness (p-wave modulus) M , bending
 modulus B of the ice and sediment thickness b . Assuming radial flow,

$$\nabla^2 = \frac{1}{r} \frac{\partial}{\partial r} r \frac{\partial}{\partial r}, \quad (13)$$

the associated flux of water q at radius r is

$$q(r) = -2\pi rT \frac{\partial h}{\partial r}, \quad (14)$$

299 and $q(r) = Q_o(t)$ is the injection flux into the subglacial environment.

300 This problem can be solved numerically for any injection flux $Q_o(t)$. By entering the time-varying injection
 301 flux for BH19g breakthrough (Section 3.1.2) into Equation 14, we predicted the response of hydraulic head
 302 at BH19e (4 m from the injection point of BH19g). An automated nonlinear optimisation procedure was
 303 used to determine the best-fit model parameters, yielding $B = 3.01 \times 10^9 \text{ Pa m}^3$, $M/b = 1 \times 10^4 \text{ Pa m}^{-1}$,
 304 $T = 1.37 \times 10^{-4} \text{ m}^2 \text{ s}^{-1}$. The prediction initially follows the data closely and it captures the initial decrease
 305 in BH19e hydraulic head as the flexural wave passes through (Fig. 4a). However, the model does not capture
 306 the subsequent development of the pressure recorded in BH19e; instead it predicts that the pressure drops
 307 off too rapidly after the first two minutes. We discuss further in Section 4.1.

308 3.2. Pumping tests

309 3.2.1. Observations

310 Following each breakthrough event, the hose was raised back to the surface over ~ 2 h (Table 1; Figs. S1-
 311 S3), with the continued supply of water into the borehole functioning as a pumping test. We captured
 312 the pressure response at the base of BH19e to such a pumping test following the breakthrough of BH19g
 313 (Fig. 5). Although water was pumped down the hose while it was raised to the surface for all boreholes
 314 that reached the bed, no other pumping tests were captured as they occurred prior to the installation of
 315 pressure sensors. During the BH19g(e) pumping test the water pressure was measured in BH19e, 4.1 m
 316 distant (Fig. 5).

317 Starting 28 min after the breakthrough of BH19g the head in BH19e increased at a steady rate of
 318 1.24 m h^{-1} (Fig. 5). This period of steady increase was interrupted by the temporary shutdown of the
 319 water supply when pressure-heater units were refuelled, with the linear increase in head resuming at the
 320 slightly higher rate of 1.36 m h^{-1} . The rate of change of hydraulic head increased again to 7.40 m h^{-1} when
 321 the drill stem and hose rose above the borehole water level, indicating that, while the stem was below the
 322 water line, part of the water pumped in to the borehole was replacing the reducing volume displaced by
 323 the hose as it was raised to the surface. We refer to these three periods of linearly increasing head as PT1,
 324 PT2 and PT3, respectively.

Discharge from the base of BH19g (Q_o) was calculated by correcting the input flux Q_i ($1.25 \times 10^{-3} \text{ m}^3 \text{ s}^{-1}$) for storage within BH19g (Q_s), and for the flux offsetting the decreasing water displacement caused by the hose as it was raised to the surface (Q_d)

$$Q_o = Q_i - Q_d - Q_s. \quad (15)$$

The pumping test was undertaken nine days after the breakthrough of BH19e. Hence, we assume that storage within BH19e was negligible due to rapid borehole refreezing within cold ice that was present above a 70 m thick basal temperate layer (Law and others, 2021). Q_d was calculated as

$$Q_d = \pi r_d^2 \bar{U}_d, \quad (16)$$

where $r_d = 0.015 \text{ m}$ is the hose radius and \bar{U}_d is the mean drill speed. For PT3, $Q_d = 0$ as the drill stem and hose were above the borehole water level. Q_s is the flux lost to storage in the injection borehole calculated from the rate of change in head dh/dt and the area of the borehole, which for PT1 and PT2 is annular as the hose was below the borehole water level

$$Q_s = (\pi r_s^2 - \pi r_d^2) \frac{dh}{dt}, \quad (17)$$

where $r_s = 0.14 \text{ m}$ is the radius of BH19g at the surface (see Appendix B). For PT3

$$Q_s = \pi r_s^2 \frac{dh}{dt}. \quad (18)$$

325 As the measurement of hydraulic head in BH19g did not start until after the pumping test, we assume
326 that the rate of change of hydraulic head was the same in BH19g and BH19e.

327 These calculations reveal that during the pumping test the vast majority (90%) of water pumped into
328 the borehole was discharged from the base (Table 2). Furthermore, this discharge from the borehole base
329 (Q_o) was remarkably steady, averaging $1.12 \times 10^{-3} \text{ m}^3 \text{ s}^{-1}$ with a standard deviation of $1.1 \times 10^{-6} \text{ m}^3 \text{ s}^{-1}$.
330 It follows that the mean velocity of the water ($\bar{U}_w = Q_o/\pi r_0^2$) through the borehole near the base during
331 all periods was also steady, averaging $3.2 \times 10^{-2} \text{ m s}^{-1}$ with a standard deviation of $3.1 \times 10^{-5} \text{ m s}^{-1}$.

To test whether the outflow of borehole water during the pumping test was laminar or turbulent we calculated the Reynolds number (Re) using Equation 4. During all periods, $Re \approx 3750$, indicating that

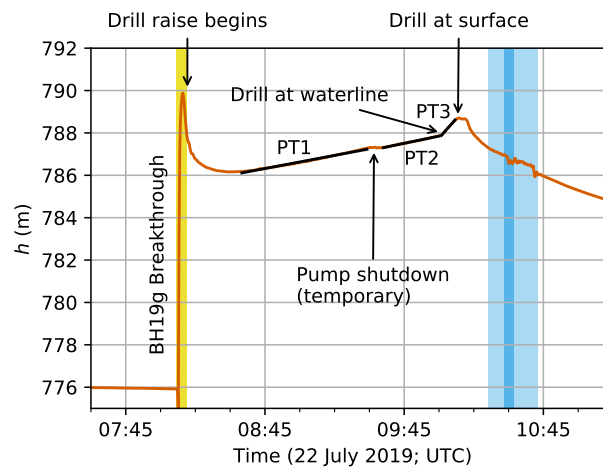


Fig. 5. Time series of BH19e hydraulic head (red line) capturing the response to BH19g breakthrough and the injection of water as the hose was raised to the surface. Post-breakthrough the drill stem was kept stationary at the bed for 4 min 39 s (yellow shading). Linear fits during the three pumping test periods are shown with black lines. The light blue shade marks the period during which a piezometer was lowered into BH19g, and the dark blue shade marks the time the piezometer was temporarily snagged (see Section 4.1 for details).

flow of water in the bottom of the borehole was turbulent during the pumping tests. If, however, we assume that water leaves the borehole through a gap of width δ the Reynolds number for flow through this gap is

$$Re = \frac{Q_o D_h \rho_w}{2\phi\pi r \delta \mu_w}, \quad (19)$$

where D_h is the hydraulic diameter of the water film, r is the distance from the borehole, and ϕ is the areal fraction of the bed occupied by the gap (Iken and others, 1996; de Marsily, 1986). For thin films with a large lateral extent D_h can be approximated as 2δ (de Marsily, 1986) and the equation can be simplified to

$$Re = \frac{Q_o \rho_w}{\phi\pi r \mu_w}. \quad (20)$$

332 Using Equation 20 and following the approach of Lüthi (1999), the transition from turbulent to laminar
 333 flow occurs at a distance of ~ 1 m from the borehole base for even the low value of $\phi = 0.1$. Hence, water
 334 flow beyond this point can be treated as laminar allowing the application of standard hydrogeological
 335 techniques.

Table 2. Statistics for the BH19g(e) pumping test. V_o is the volume of water discharged from the borehole base during the period. All other symbols are defined in the text.

Period	PT1	PT2	PT3
Time since breakthrough (h)	0.9	1.7	1.9
Duration (min)	54	24	6
s (m)	11.2	12.1	12.8
dh/dt (m h ⁻¹)	1.24	1.36	7.40
\bar{U}_d (m min ⁻¹)	8.80	8.82	8.75
Q_i (10 ⁻⁴ m ³ s ⁻¹)	12.5	12.5	12.5
Q_d (10 ⁻⁴ m ³ s ⁻¹)	1.04	1.04	0
Q_s (10 ⁻⁴ m ³ s ⁻¹)	0.210	0.231	1.27
Q_o (10 ⁻⁴ m ³ s ⁻¹)	11.3	11.2	11.2
Q_o (% of Q_i)	90.0	89.8	89.8
V_o (m ³)	3.65	1.62	0.41
T_s^* (10 ⁻⁵ m ² s ⁻¹)	1.51 – 4.75	1.39 – 4.37	1.31 – 4.13
T^\dagger (10 ⁻⁵ m ² s ⁻¹)	7.96	3.93	0.62

*Calculated using the Thiem (1906) method (Eq. 21)

†Calculated using the analytical solution to the simplified

Hewitt and others (2018) model (Eq. 23b)

3.2.2. Hydraulic transmissivity according to the Thiem method

The hydraulic transmissivity (T_s) of a subglacial sediment layer can be calculated by applying the Thiem (1906) method to the pumping test data. The Thiem method assumes that a steady state has been reached within a vertically-confined, homogeneous, isotropic, and incompressible aquifer with Darcian flow. In these limits the hydraulic transmissivity

$$T_s = \frac{Q_o}{2\pi s} \ln \frac{R}{r}, \quad (21)$$

where $r = 4.1$ m is the horizontal distance between the injection borehole (BH19g) and the monitoring borehole (BH19e), and $s = h - h_0$, is the mean hydraulic head (h) during the pumping test above the reference head (h_0). The radius of influence (R) is the distance to the theoretical point at which the hydraulic head remains unchanged at the equilibrium level (that is, at radial distance R , $h = h_0$; $s = 0$; Fig. 2). (Note that the subscript in T_s indicates that the method used assumes Darcian flow through

342 sediment rather than through a gap at the ice-sediment interface, later denoted T_g , or some combination
 343 of the two, for which we use T to represent the effective transmissivity.) The strong response of hydraulic
 344 head in BH19e to breakthrough in BH19g and the close agreement between head in these boreholes during
 345 the recovery phase (Fig. 3) indicates the radius of influence is greater than the distance between BH19e and
 346 BH19g, which is 4.1 m at the surface. On the other hand, assuming a homogeneous, isotropic aquifer, the
 347 lack of a positive pressure peak in BH19c suggests the radius of influence is less than 70 m. Using Equation
 348 10, and reasonable R values of 10 and 70 m gives hydraulic transmissivity from $(1.31 - 4.75) \times 10^{-5} \text{ m}^2 \text{ s}^{-1}$
 349 (Table 2).

350 Although the Thiem (1906) method is well established it has limitations. The first is that the radius of
 351 influence R is difficult to interpret physically. The second is the requirement that a steady state has been
 352 reached. A third limitation in our application is that to calculate the flux of water leaving the base of the
 353 injection borehole (BH19g) we assume that the rate of change in hydraulic head is the same in BH19g as
 354 that recorded in BH19e.

355 3.2.3. Hydraulic transmissivity according to the Hewitt model

An alternative method to calculate the transmissivity from the pumping test data is through the application
 of an analytical solution to the simplified Hewitt and others (2018) model. During the pumping test Q_o is
 steady, thereby permitting an asymptotic solution of Equation 12 that, based on the monitoring borehole
 at radius r being sufficiently near to the injection borehole, gives

$$h(r) \rightarrow -\frac{Q_o}{2\pi T} \ln \left(r \sqrt{\frac{\rho g}{A_1 t}} \right). \quad (22)$$

Hence, the predicted rate of change in hydraulic head at the nearby monitoring borehole is:

$$\frac{\partial h}{\partial t} \rightarrow \frac{Q_o}{4\pi T t} \implies T = \frac{Q_o}{4\pi t} \left(\frac{\partial h}{\partial t} \right)^{-1}. \quad (23a,b)$$

356 This expression is independent of parameters B , M , and b and is sensitive only to the transmissivity. In
 357 principle this provides an alternative means of predicting T from the measured rate of change in hydraulic
 358 head during the pumping test, which avoids the limitations of the Thiem (1906) method outlined in
 359 Section 3.2.2. This method (Eq. 23b) gives estimates of T decreasing from $7.96 \times 10^{-5} \text{ m}^2 \text{ s}^{-1}$ during PT1,
 360 to $3.93 \times 10^{-5} \text{ m}^2 \text{ s}^{-1}$ during PT2, to $0.62 \times 10^{-5} \text{ m}^2 \text{ s}^{-1}$ during PT3 (Table 2).

361 3.3. Recovery tests

362 3.3.1. Observations

363 After water input to the borehole ceased, the borehole water pressure recovered to the reference head (h_0)
 364 over $\sim 36 - 50$ h (Fig. 3b; Table 1). The range in recovery times can be explained by the variable timing
 365 and magnitude of the diurnal cycle in subglacial water pressure (Fig. 3). The observed recovery curves
 366 were similar (Fig. 3b) suggesting spatially uniform subglacial hydrological conditions between boreholes.
 367 We analysed the early phase of the recovery by fitting an exponential decay curve (Weertman, 1970, 1972;
 368 Engelhardt and Kamb, 1997) and the late phase using the Cooper and Jacob (1946) recovery test method.
 369 This provides us with two further estimates of hydraulic transmissivity: the first at 4–5 h post-breakthrough
 370 (early-phase), and the second at 14 – 27 h post-breakthrough (late-phase).

371 3.3.2. Exponential decay curve

The early phase of the recovery curve can be approximated as an exponential decay using the water-film
 model of Weertman (1970, 1972):

$$s(t) = s_0 \exp \frac{-t}{D}, \quad (24)$$

372 where s_0 is the initial recharge at the time the pumps stopped, t is the time since the pumps stopped,
 373 and D is a time constant determined by log-linear fitting (Fig. 6a-c). The water-film model, which is
 374 referred to as the gap-conduit model in Engelhardt and Kamb (1997), is based on the Hagen-Poiseuille
 375 equation and assumes laminar flow through a constant-width gap at the interface between the ice and a
 376 level, impermeable bed.

In the recovery curves of tests BH19c and BH19e the first part of the curve is missing due to the time
 taken to lower the pressure transducer to the bed after the drill stem was raised to the surface (Fig. 3a).
 Hence, s_0 was also treated as an unknown. In the BH19g(e) test the monitoring borehole was different
 from the injection borehole and the first part of the recovery curve was recorded. The initial BH19g(e)
 recovery curve was not, however, exponential and linear-log fitting was delayed for 5000 s (83 min; Fig. 6c).
 After this delay the trend for BH19g(e) was quasi-exponential, in common with the other tests, and s_0
 was again treated as an unknown for this test (Fig. 6a-c). Hence, measured s_0 for BH19g(e) is 12.7 m and
 that calculated by fitting Equation 24 is 10.1 m. The resulting time constant D was 18,200 s for BH19c,
 25,000 s for BH19e, and 23,000 s for BH19g(e). Rearranging Equation 9 of Engelhardt and Kamb (1997)

allows the gap width δ to be calculated from the time constant as

$$\delta = \left(\frac{6\mu_w r_s^2}{D\rho_w g\phi} \ln \frac{R}{r_0} \right)^{1/3}. \quad (25)$$

Furthermore, if we make the reasonable assumption of laminar flow at a distances > 1 m from the borehole (Section 3.2), the transmissivity (T_g) of a continuous porous medium equivalent to a gap of width δ is given by de Marsily (1986) as

$$T_g = \delta^3 \frac{\phi g \rho_w}{12\mu_w}. \quad (26)$$

Combining Equations 25 and 26 (see Appendix A) allows T_g to be calculated directly from the time constant (D)

$$T_g = \frac{r_s^2}{2D} \ln \frac{R}{r_0}. \quad (27)$$

377 For each test, two values of transmissivity were calculated, bracketing the radius of influence R to 10–70 m.
 378 The results show that hydraulic transmissivity was an order of magnitude lower during the early recovery
 379 phase than during the pumping test, with hydraulic transmissivity spanning the range $(1.8 - 3.5) \times$
 380 10^{-6} m s^{-1} equivalent to gap widths of 0.16 – 0.20 mm for gaps covering the whole of the glacier bed
 381 ($\phi = 1$; Table 3).

Table 3. Results from the gap-conduit model (exponential fit). Gap width and the apparent hydraulic transmissivity were calculated for two values of the radius of influence ($R = 10$ and 70 m). Gap widths were additionally calculated for two areal fractions of the bed covered by the gap ($\phi = 0.1$ and 1.0). The apparent gap transmissivity is independent of ϕ because gap cross-sectional area is a product of δ and ϕ .

Test	s_0 (m)	D (s)	δ (mm)		T_g (10^{-5} m s^{-1})
			$\phi = 1$	$\phi = 0.1$	
BH19c	16	18,200	0.18 – 0.20	0.38 – 0.43	0.25 – 0.35
BH19e	14.8	25,000	0.16 – 0.18	0.34 – 0.38	0.18 – 0.26
BH19g(e)	10.1	23,000	0.16 – 0.18	0.35 – 0.39	0.19 – 0.28

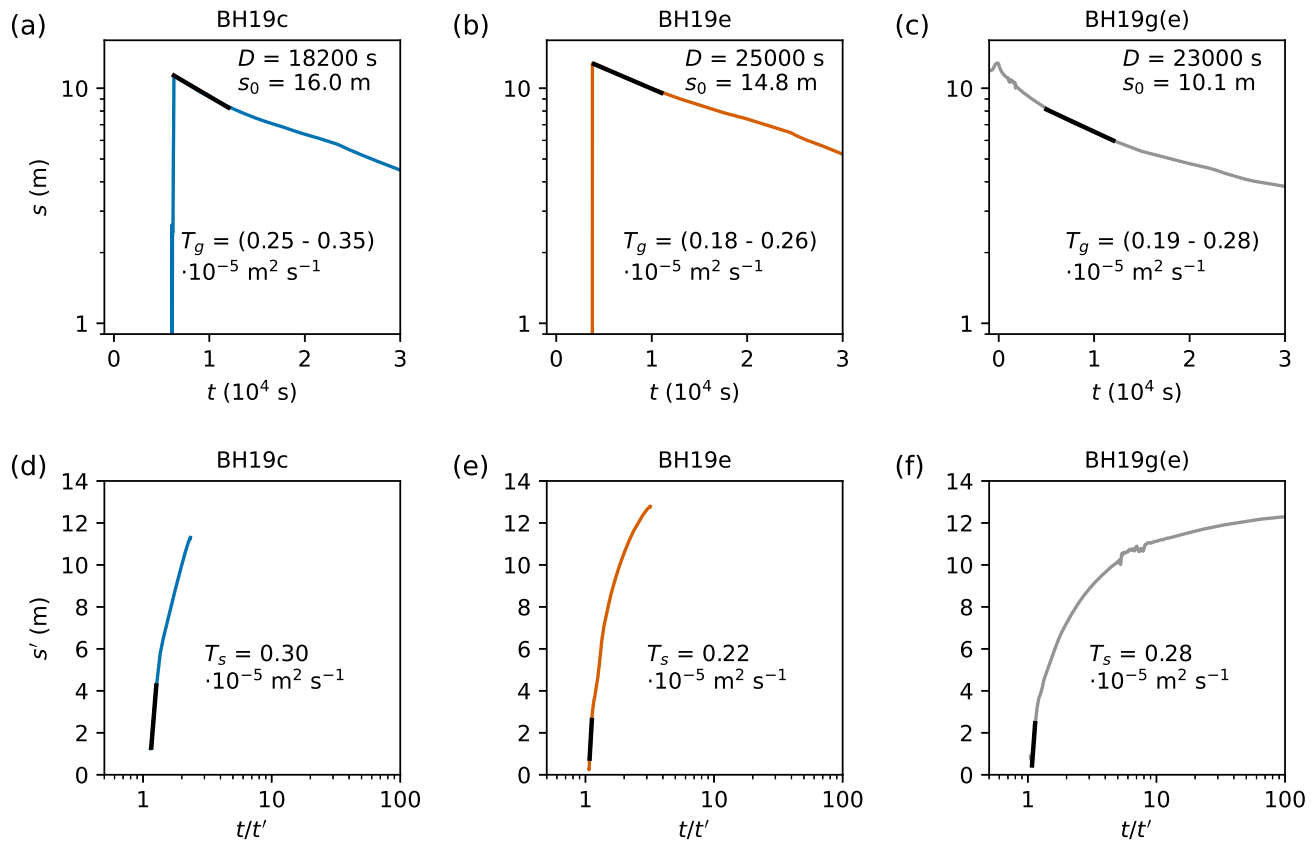


Fig. 6. Recovery tests including: (a-c) exponential fits (black) applied to the early stage of recovery curves plotted as hydraulic head above background (s) on the logarithmic y-axis against time (t); and (d-e) Cooper and Jacob (1946) recovery test linear-log fitting (black) applied to the late stage of the recovery curves plotted as residual drawdown (s') against the logarithm of the time ratio (t/t').

382 3.3.3. Cooper and Jacob recovery tests

Hydraulic transmissivity can also be derived from the later stages of the recovery curve using the Cooper and Jacob (1946) recovery test method, providing information about the hydrologic nature of the basal condition as it returns to its original state. This method is based on the observation that, after a certain period of time, drawdown (or in our case recharge) within an aquifer at a given distance from a borehole decreases approximately in proportion to the logarithm of time since the discharge began. The method assumes a non-leaky, vertically-confined aquifer of infinite lateral extent and a steady rate of discharge. Although the Theis (1935) method — on which the Cooper and Jacob (1946) method is based — requires a constant pumping rate, the method can be applied to a recovery test (i.e. after the pumps have ceased) using the principle of superposition of drawdown (e.g. de Marsily, 1986; Hiscock and Bense, 2014). Under this principle, pumping is assumed to continue uninterrupted while a hypothetical drawdown well is superimposed on the

monitoring well from the time pumping stopped to exactly counteract the recharge from the pump. The residual recharge s' is

$$s' = h - h_0 = \frac{Q}{4\pi T} [W(u) - W(u')], \quad (28)$$

where h , h_0 , Q and T are as previously defined and $W(u)$ and $W(u')$ are well functions for the real and hypothetical boreholes where

$$u = \frac{r^2 S}{4Tt}, \quad u' = \frac{r^2 S}{4Tt'}, \quad (29a,b)$$

and S is the storage coefficient, which cannot be determined using this method. In the previous two equations, t is time since the start of pumping, which for our tests is at breakthrough, and t' is the time since the pumps stopped. As per the standard Cooper and Jacob (1946) method for pumping tests, for small values of u' and large values of t' , the well functions can be approximated so that residual recharge can be estimated from the simplified equation

$$s' = \frac{2.303Q}{4\pi T} \log_{10} \frac{t}{t'}. \quad (30)$$

Hence, linear-log fitting allows hydraulic transmissivity (T_s) to be calculated,

$$T_s = \frac{2.303Q}{4\pi \Delta s'}, \quad (31)$$

383 where $\Delta s'$ is the rate of change of residual recharge with respect to the logarithmic time ratio. The Cooper
 384 and Jacob (1946) recovery test method described above has the advantage that the rate of recharge can
 385 be assumed to be constant, in contrast to the discharge during an actual pumping test, which may vary
 386 (Hiscock and Bense, 2014).

387 During the recovery phase, the sampling interval was increased from 5 s to 300 s. Prior to application
 388 of the Cooper and Jacob (1946) recovery test method, the data were resampled to a constant 5 s interval
 389 and interpolated linearly. The data presented in Figure 6d-f extends from the time of pressure transducer
 390 installation at the bed (or in the case of BH19g the earlier time at which the pumps were stopped),
 391 to when diurnal pressure variations began. Fitting was applied to the later stages of the recovery curve
 392 where the trend in recharge versus the logarithmic time ratio was linear, as is required for this method to be
 393 appropriate. Accordingly, hydraulic transmissivity was calculated to be $3.0 \times 10^{-6} \text{ m}^2 \text{ s}^{-1}$, $2.2 \times 10^{-6} \text{ m}^2 \text{ s}^{-1}$
 394 and $2.8 \times 10^{-6} \text{ m}^2 \text{ s}^{-1}$ for BH19c, BH19e, and BH19g respectively.

Table 4. Summary of borehole response test results in chronological order with respect to time breakthrough (t).

Test	Type (period)	Method	t (h)	δ (mm)		T ($10^{-5} \text{ m}^2 \text{ s}^{-1}$)
				$\phi = 1$	$\phi = 0.1$	
BH19g(e)	Breakthrough	Hewitt and others (2018)*	0	0.67	1.44	13.70
BH19g(e)	Pumping (PT1)	Thiem (1906)	0.9	0.32 – 0.47	0.69 – 1.01	1.51 – 4.75
BH19g(e)	Pumping (PT1)	Hewitt and others (2018)†	0.9	0.56	1.21	7.96
BH19g(e)	Pumping (PT2)	Thiem (1906)	1.7	0.31 – 0.46	0.67 – 0.99	1.39 – 4.37
BH19g(e)	Pumping (PT2)	Hewitt and others (2018)†	1.7	0.44	0.95	3.93
BH19g(e)	Pumping (PT3)	Thiem (1906)	1.9	0.31 – 0.45	0.66 – 0.97	1.31 – 4.13
BH19g(e)	Pumping (PT3)	Hewitt and others (2018)†	1.9	0.24	0.51	0.62
BH19c	Recovery (early)	Weertman (1970) exponential fit	4.9	0.18 – 0.20	0.38 – 0.43	0.25 – 0.35
BH19e	Recovery (early)	Weertman (1970) exponential fit	4.4	0.16 – 0.18	0.34 – 0.38	0.18 – 0.26
BH19g(e)	Recovery (early)	Weertman (1970) exponential fit	4.4	0.16 – 0.18	0.35 – 0.39	0.19 – 0.28
BH19c	Recovery (late)	Cooper and Jacob (1946)	14.1	0.19	0.40	0.30
BH19e	Recovery (late)	Cooper and Jacob (1946)	27.2	0.17	0.36	0.22
BH19g(e)	Recovery (late)	Cooper and Jacob (1946)	23.0	0.18	0.39	0.28

*Reduced model (Eq. 14)

†Analytical solution (Eq. 23b)

395 4. DISCUSSION

396 4.1. Hydraulic ice-sediment separation

397 The average drop in borehole water level during breakthrough indicates that the subglacial environment
398 accommodated 4.70 m^3 of water within 200 s. For all three boreholes that reached the bed, the delayed
399 recovery to background levels over 36 – 50 h suggests that this breakthrough water and an additional
400 $\sim 10 \text{ m}^3$ of water injected during the raise, could not be efficiently drained away from the immediate
401 vicinity of the borehole's base. For example, recovery to the reference head took 45 h following the input
402 of 13.6 m^3 of water injected into BH19g at breakthrough and during the drill stem raise (Table 1; Fig.
403 3b) yielding a mean discharge of $8.4 \times 10^{-5} \text{ m}^3 \text{ s}^{-1}$. If the boreholes had intercepted a conduit with the
404 capacity to drain the water away efficiently then the mean discharge rate would have been higher and the
405 recovery time would have been shorter. Hence, it follows that at least some of this water must have been
406 temporarily stored locally. We hypothesise that water was predominantly stored within a gap opened up

407 at the ice-sediment interface facilitated by the overpressure (913 ± 101 kPa; Table 1) exerted at the base of
 408 water-filled boreholes due to the greater density of water than ice. In the following analysis we constrain
 409 the geometry of this gap and investigate how the gap width changed through time.

410 An approximate calculation of the plausible range in gap width can be made for the BH19g breakthrough
 411 by assuming a uniform cylindrical subglacial water sheet with a radius ranging from 10 – 70 m (that is just
 412 greater than the distance to BH19e where a positive peak in pressure was observed and just less than the
 413 distance to BH19c where there was no positive peak in pressure). Under these assumptions, a gap width of
 414 0.3 – 16.5 mm could accommodate the 5.17 m^3 of water injected in 200 s after BH19g breakthrough. This
 415 range is consistent with a lack of discernible ice surface uplift in data collected by a GNSS receiver at R30,
 416 confirming that surface uplift was below the precision of the GNSS data of ± 50 mm (Fig. S4). Assuming a
 417 straight-sided cylinder with a volume equal to that injected during BH19g of 5.17 m^3 the upper bound on
 418 the surface uplift of 50 mm provides a lower bound on the radius of the uplift of ~ 5.7 m.

Further estimates of gap widths can be determined from the hydraulic transmissivity measurements. If we assume laminar flow, which is reasonable at distances > 1 m from the borehole (see Section 3.2), the gap width (δ), equivalent to a continuous porous medium with an effective hydraulic transmissivity (T_g), is given by rearranging Equation 26

$$\delta = \left(\frac{12T_g\mu_w}{\phi\rho_w g} \right)^{1/3}. \quad (32)$$

419 Assuming the gap is uniformly distributed across the bed ($\phi=1$) these estimates show a decrease from
 420 0.67 mm during breakthrough to a mean of 0.18 mm during the recovery phase (Table 4; Fig. 7). A
 421 comparable trend was measured by Lüthi (1999) using similar methods on Sermeq Kujalleq (Jakobshavn
 422 Isbræ), with gap widths decreasing from 0.7 – 0.9 mm during a pumping test to 0.5 mm during the recovery
 423 phase. We interpret this decrease in hydraulic transmissivity and equivalent gap widths with time since
 424 breakthrough (Fig. 7) as evidence for progressive closure of gaps opened at the ice-sediment interface
 425 (in response to decreasing hydraulic head). Both our estimates and those of Lüthi (1999) are lower than
 426 those of 1.4 – 2.0 mm estimated from boreholes drilled on Whillans Ice Stream (formerly Ice Stream B) in
 427 West Antarctica; however, this may, at least partly, be explained by the earlier timing made possible by
 428 measuring pressure within the Whillans boreholes while they were drilled (Engelhardt and Kamb, 1997).
 429 The areal extent of the gap exerts a relatively weak control on gap width, with gap width approximately
 430 doubling for gaps occupying just one tenth of the bed ($\phi = 0.1$; Table 4; Fig. 7). Other lines of evidence
 431 that support the gap opening hypothesis are discussed below.

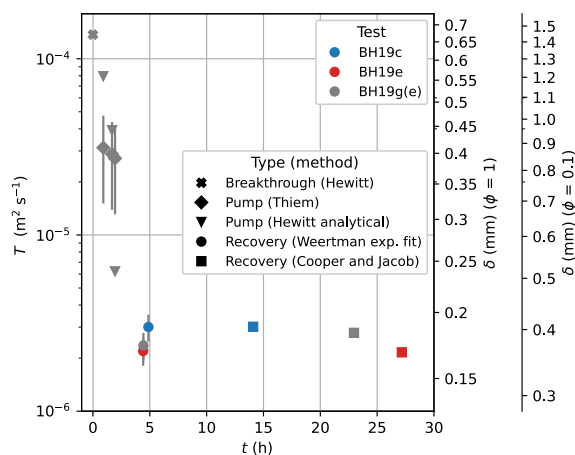


Fig. 7. Hydraulic transmissivity (T) from multiple tests and methods plotted against time (t) since respective breakthrough. The equivalent gap width (δ) is shown on the right-hand axes for gaps covering a range of fractions of the bed ($\phi = 1$ and $\phi = 0.1$). Where appropriate, the range in the hydraulic transmissivity derived using radius of influence $R = 10 - 70$ m is shown by error bars.

432 The initial drop in hydraulic head in BH19e was punctuated by a 14 m increase after 20 ± 5 s, which we
 433 interpret to be the arrival of the water from the BH19g breakthrough event through a gap opened at the
 434 ice-sediment interface. The delayed arrival of the pressure increase demonstrates that no efficient hydraulic
 435 connection existed between BH19e and BH19g prior to the breakthrough of BH19g. The 20 ± 5 s delay
 436 between the start of the load increase on the drill tower and the start of the pressure increase in BH19e
 437 gives a mean velocity of the pressure pulse of 0.20 ± 0.04 m s⁻¹. Similar pressure pulse propagation velocities
 438 of $0.08 - 0.18$ m s⁻¹ were observed on Whillans Ice Stream (Engelhardt and Kamb, 1997). If a conduit existed
 439 between BH19g and BH19e prior to breakthrough, the pressure pulse would be transmitted at the speed
 440 of sound (1440 m s⁻¹) and attenuated in amplitude by the viscosity of water at a rate proportional to the
 441 gap width (Engelhardt and Kamb, 1997). The observed delay of 20 ± 5 s is four orders of magnitude longer
 442 than the expected delay of a sound wave through 4.1 m of water of 0.003 s, which confirms that no conduit
 443 existed between BH19g and BH19e prior to breakthrough. Instead, we infer that the delay represents the
 444 propagation velocity of the gap tip outwards from BH19g.

445 On the other hand, the disturbance in hydraulic head in BH19e caused by attempts to free a piezometer
 446 snagged at 394 m depth in BH19g, demonstrates that a hydraulic connection between the two boreholes
 447 was present at this time 2.4 h after breakthrough (Fig. 5). The piezometer in BH19g was freed after
 448 repeated pulling on the cable, which caused the hydraulic head to fluctuate in BH19e, with disturbance

449 continuing as the piezometer was lowered to the bed. We infer that this inter-borehole transmission of
450 pressure perturbations indicates an open gap at the ice-sediment interface at this time.

451 The performance of the simplified Hewitt and others (2018) model in predicting the pressure response to
452 borehole breakthrough provides further evidence for gap opening. The simplified model makes a reasonable
453 prediction of the initial pressure response in BH19e to BH19g breakthrough (Fig. 4). The model closely
454 reproduces the small (0.93 m) drop in hydraulic head followed by the rapid rise within the first minute.
455 This suggests that the small drop in BH19e pressure can be explained by the propagation of a flexural wave
456 through the ice that is faster than the spread of water. Furthermore, the initial drop in pressure indicates
457 that the sediment is deformable because such a drop cannot be reproduced by the model if the sediment is
458 rigid (see Figure 7b of Hewitt and others, 2018). We can also exclude gap opening via fracturing at the ice-
459 sediment interface because fracturing would be characterised by an abrupt positive pressure pulse without
460 an initial drop. The model, however, predicts that the hydraulic head should reduce much more rapidly
461 after the peak than was observed. Furthermore the analytical solution to the model (Eq. 23b) predicts that
462 $\partial h/\partial t$ should decrease non-linearly as $1/t$, whereas the measured linear trends in hydraulic head during
463 the pumping test suggest that $\partial h/\partial t$ was constant (Fig. 5). Both these disparities can be explained by
464 the progressive closure of a gap opened at the ice-sediment interface resulting in the effective hydraulic
465 transmissivity decreasing through time, as was measured (Table 4; Fig. 7). The simplified model applied
466 here does not include gap opening and instead assumes a constant effective transmissivity for each pumping
467 test period. Indeed, the effective transmissivity predicted by the analytical solution becomes progressively
468 smaller from PT1 to PT3 (Table 4; Fig. 7), which supports the hypothesis of gradual gap closure.

469 The observation of an instantaneous drop in hydraulic head of 0.11 m in BH19c in response to BH19g
470 breakthrough without a subsequent increase in head (Fig. 4a) also cannot be reproduced by the simplified
471 model; the model predicts a flexural wave that would be apparent at any fixed radius as a small pressure
472 drop followed by a large pressure rise. We hypothesise that the drop in pressure in BH19c is caused
473 by elastic uplift at the BH19g injection site increasing the volume of a hydraulically-isolated cavity at
474 BH19c, and that cavity expansion without an increase in water mass leads to a reduction in water density
475 and pressure — that is a rarefaction. The simplified Hewitt and others (2018) model cannot reproduce
476 rarefactions caused by stress transfer through the ice because it assumes that water compressibility is
477 zero and, more fundamentally, it directly couples vertical displacement of the ice to the pressure in the
478 subglacial environment, so that cavity expansion cannot occur without an increase in pressure (and vice

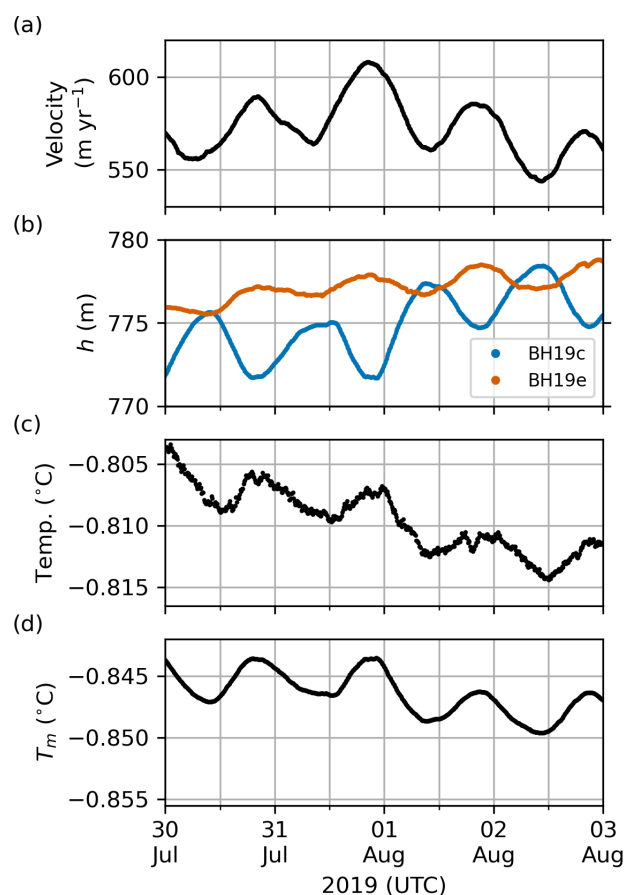


Fig. 8. Time series of (a) horizontal ice velocity, (b) hydraulic head in BH19c and BH19e, (c) temperature at the base of BH19c, and (d) pressure-dependent melting temperature T_m calculated from the water pressure recorded in BH19c. Note that although the y-axes for (c) and (d) are offset the y-axis range is identical for both. The offset between measured temperature and T_m can be explained by uncertainties in the sensor installation depths and the Clausius-Clapeyron gradient.

479 versa). Further evidence for hydraulic isolation of the BH19c cavity is provided by diurnal water pressure
 480 variations that are anti-correlated with those in BH19e and ice velocity (Fig. 8a,b; e.g. Murray and Clarke,
 481 1995; Meierbachtol and others, 2016; Lefeuvre and others, 2018). Further evidence for BH19c cavity isolation
 482 is provided by the observation that diurnal pressure variations in BH19c are manifested as small ($\sim 0.05^{\circ}\text{C}$
 483 peak-to-peak) temperature cycles recorded at the base of BH19c (Fig. 8). This demonstrates that the water
 484 temperature quickly equilibrates with the pressure-dependent ice temperature, which would occur within
 485 an isolated cavity but not in a connected conduit. We would expect that within a connected conduit a
 486 throughput of water from different regions of the bed at variable pressures and temperatures would mask
 487 the small pressure-driven diurnal variations in temperature.

Rearranging the equation of state for water assuming mass is conserved and that temperature is constant, allows the pressure change to be related to the change in cavity volume

$$\frac{V}{V_0} = \frac{1}{\exp[\beta_w(p_w - p_{w0})]}, \quad (33)$$

488 where V_0 and p_{w0} are the reference volume and pressure and $\beta_w = 5.1 \times 10^{-10} \text{ Pa}^{-1}$ is the compressibility
 489 of water. We can constrain the initial cavity geometry in two situations. First, the observation of no prior
 490 hydraulic connection between BH19e and BH19g, which were separated at the surface by 4.1 m, indicates
 491 the BH19e cavity was smaller than this distance. Second, the volume of water drained during BH19c
 492 breakthrough and the hose raise of 15.6 m^3 provides an approximate maximum constraint on the BH19c
 493 cavity volume. These constraints are consistent with measurements of dye dilution in boreholes drilled
 494 on Isunnguata Sermia, which indicated cavity volumes of $7.6 \pm 6.7 \text{ m}^3$ (Meierbachtol and others, 2016).
 495 Assuming the initial BH19c cavity volume was within the reasonable range of $0.5 - 15 \text{ m}^3$ the small 0.11 m
 496 decrease in hydraulic head measured in BH19c located $\sim 70 \text{ m}$ distant can be explained by the contraction of
 497 the BH19c cavity of $0.3 - 8.2 \times 10^{-6} \text{ m}^3$. This demonstrates that, due to the low compressibility of water, the
 498 0.11 m head decrease can be explained by a small cavity contraction of $5.5 \times 10^{-5}\%$. Hence, we hypothesise
 499 that hydraulic ice-sediment separation caused by the overpressure at the base of BH19g caused elastic
 500 uplift of the BH19c cavity roof. The 0.11 m pressure drop in BH19c in response to BH19g breakthrough
 501 therefore provides direct evidence for the hypothesis of Murray and Clarke (1995) that pressure variations
 502 in hydraulically-isolated cavities occur due to elastic displacement of the ice roof driven by perturbations
 503 in hydraulically-connected regions of the bed. We discuss this further in Section 4.3.

504 4.2. Hydraulic conductivity of subglacial sediments

505 We interpret the decrease in hydraulic transmissivity with time since breakthrough (Table 4; Fig. 7) as
 506 evidence for the closure of a gap at the ice-sediment interface that was opened by the overpressure at
 507 borehole breakthrough. It is notable that hydraulic transmissivity derived using the Cooper and Jacob
 508 (1946) recovery tests were relatively constant (that is within $8 \times 10^{-7} \text{ m}^2 \text{ s}^{-1}$), despite the tests occurring
 509 over a wide range in time since breakthrough (14.1 – 27.2 h; Table 4; Fig. 7). Hence, these tests may be
 510 representative of Darcian flow through the sediment layer after gap closure. This suggestion is supported
 511 by the observation that the drawdown decreased logarithmically through time (Fig. 6d-e) as is expected
 512 under Darcian flow, which is unlikely to be the case if gap closure was incomplete. Darcian flow through
 513 subglacial sediments was also inferred at site S30 from the initially logarithmic recovery in subglacial water

514 electrical conductivity (EC) observed over 12 h following the dilution effect caused by drilling with low EC
 515 surface waters (Doyle and others, 2018).

When there is no flow through a gap at the ice-sediment interface, hydraulic transmissivity (T) is the hydraulic conductivity (K) integrated over the sediment thickness b

$$T = bK. \quad (34)$$

516 The sediment thickness at the borehole location has been estimated at 20_{-2}^{+17} m by fibre-optic distributed
 517 acoustic seismics in BH19c (Booth and others, 2020). The full sediment thickness represents an upper limit
 518 for the calculation of hydraulic conductivity due to an increase in sediment compaction with depth, and
 519 the pressure-dependent depth limit to the diffusion of water from the ice-sediment interface (Tulaczyk and
 520 others, 2000). For the range of hydraulic transmissivity from the Cooper and Jacob (1946) recovery tests
 521 of $(2.2 - 3.0) \times 10^{-6} \text{ m}^2 \text{ s}^{-1}$ (Table 4), and a range of reasonable 'hydraulically-active' sediment thicknesses
 522 of 2 – 20 m, the hydraulic conductivity is $(0.1 - 1.5) \times 10^{-6} \text{ m s}^{-1}$. This estimate is reasonable and within
 523 the range of hydraulic conductivities of glacial tills found in a range of settings by previous studies (Table
 524 5). The Cooper and Jacob (1946) recovery test for BH19c was performed several hours earlier with respect
 525 to the time of breakthrough than those in BH19e and BH19g (Fig. 7) due to the earlier establishment
 526 of diurnal pressure variations in BH19c (Fig. 3b). If gap closure was still taking place, this earlier timing
 527 could explain the slightly higher transmissivity derived for BH19c. As we cannot be certain of complete
 528 gap closure, we interpret our estimates to represent an upper bound on the hydraulic conductivity of the
 529 sediment beneath this site.

530 Our inferred sediment hydraulic conductivity is two orders of magnitude higher than that determined
 531 from laboratory analysis of sediment retrieved from beneath Whillans Ice Stream (Engelhardt and others,
 532 1990) and Trapridge Glacier in Canada (Murray and Clarke, 1995), see Table 5. A hydraulic conductivity of
 533 $10^{-7} - 10^{-6} \text{ m s}^{-1}$ is, however, broadly consistent with the type of glaciogenic sediment within core samples
 534 taken from Uummannaq Fjord. These core samples comprise glaciomarine sediments deposited during the
 535 last glacial maxima including matrix supported diamict with angular to sub-angular clasts of basalt and
 536 granitic gneiss dispersed throughout a sandy mud matrix (Ó'Coifh and others, 2013). It is therefore to
 537 be expected that the hydraulic conductivity of sediment beneath Sermeq Kujalleq (Store Glacier) in West
 538 Greenland is greater than that of fine-grained sediments underlying West Antarctic ice streams which erode
 539 soft marine sediments.

540 Laboratory measurements of the hydraulic conductivity of glacial sediments, which inherently measure
541 only Darcian flow, are typically a few orders of magnitude lower than field measurements (Table 5; Hubbard
542 and Maltman, 2000), a disparity that could be, at least partly, explained by residual gap opening at the ice-
543 sediment interface during borehole response tests (e.g. Fountain, 1994; Stone and others, 1997). Similarly,
544 in situ analysis of surface-exposures of glacial tills also tend to overestimate hydraulic conductivity relative
545 to laboratory experiments (Table 5) due to post-depositional processes such as fracturing (e.g. Haldorsen
546 and Krüger, 1990). While in-situ measurement of hydraulic conductivity of subglacial sediments appears to
547 overestimate hydraulic conductivity under strict Darcian flow conditions, laboratory measurements provide
548 little insight into the complexity of subglacial hydrological processes such as ice-sediment separation.
549 Furthermore, as glacial sediment is by nature poorly sorted, with grain sizes ranging from boulders to
550 clays, analysing samples that are large enough to be representative in laboratory experiments conducted
551 at the scale necessary is more difficult than conducting in situ measurements (Clarke, 1987; Hubbard and
552 Maltman, 2000). True subglacial water flow at this site may neither occur as entirely Darcian (laminar)
553 flow through a homogeneous, isotropic sediment layer nor exclusively through a gap at the ice-sediment
554 interface, but rather a combination of the two. In any case, our in situ measurements represent a constraint
555 on the effective hydraulic transmissivity that is independent of the process of water flow.

556 4.3. Implications for subglacial hydrology and basal motion

557 Subglacial water flow at glaciers underlain by porous sediment will naturally occur as laminar Darcian flow
558 through interconnected pore spaces, although only insofar as the hydraulic transmissivity of the sediment
559 is sufficient to accommodate the input of meltwater. With sustained inputs of water to the bed of many
560 glaciers, from surface melt for example, it may also be natural for a portion of that input to be stored
561 temporarily in gaps opened elastically at the ice-sediment interface, when water is delivered faster than it
562 can permeate into the sediment below. The evidence presented herein demonstrates that the overpressure
563 of a water-filled borehole can open a gap at the ice-sediment interface and need not directly intersect an
564 active subglacial drainage system in order to drain. The delayed arrival of the pressure pulse in BH19e rules
565 out the existence of sheet flow (Weertman, 1970; Alley and others, 1989; Creyts and Schoof, 2009), efficient
566 conduits such as R-channels or canals (e.g. Röthlisberger, 1972; Walder and Fowler, 1994; Ng, 2000), and
567 linked cavities (e.g. Kamb, 1987) prior to BH19g breakthrough, but supports the gap-opening theory of
568 Engelhardt and Kamb (1997). We infer that prior to the breakthrough of BH19g, subglacial drainage at this

Table 5. Selected hydraulic conductivities of glacial sediments from the literature in ascending order. Sediments at the lower end of the scale ($K \leq 10^{-4} \text{ m s}^{-1}$) were typically interpreted as unconsolidated sands and gravels, often associated with subglacial channels.

K (m s^{-1})	Location (method)	Source
$10^{-12} - 10^{-6}$	Literature review of glacial tills	Freeze and Cherry (1979)
$10^{-12} - 10^{-9}$	Haut Glacier d'Arolla, Switzerland (laboratory measurement)	Hubbard and Maltman (2000)
$10^{-11} - 10^{-9}$	Coastal exposure of glacial till, Traeth y Mwnt, Wales (laboratory measurement)	Hubbard and Maltman (2000)
10^{-9}	Whillans Ice Stream, Antarctica (laboratory measurement)	Engelhardt and others (1990)
10^{-9}	Trapridge Glacier, Canada (analysis of pressure freezing curves)	Waddington and Clarke (1995)
$10^{-9} - 10^{-8}$	Storglaciaren, Sweden (ploughmeter tests)	Fischer and others (1998)
10^{-8}	Storglaciaren, Sweden (laboratory measurement)	Iverson and others (1994)
10^{-8}	Trapridge Glacier, Canada (laboratory measurement)	Murray and Clarke (1995)
$10^{-7} - 10^{-6}$	Sermeq Kujalleq (Store Glacier), Greenland (borehole response tests)	This study
$10^{-7} - 10^{-5}$	Surface-exposures of glacial till, Snowy Range, Wyoming (infiltration tests)	Ronayne and others (2012)
$10^{-7} - 10^{-4}$	Haut Glacier d'Arolla, Switzerland (diurnal pressure wave propagation)	Hubbard and others (1995)
$10^{-7} - 10^{-4}$	South Cascade Glacier, USA (diurnal pressure wave propagation)	Fountain (1994)
10^{-6}	Breidamerkurjökull, Iceland (laboratory measurement)	Boulton and Dent (1974)
10^{-5}	Midre Lovénbreen, Svalbard (slug tests)	Kulesa and Murray (2003)
10^{-4}	Trapridge Glacier, Canada (breakthrough response tests)	Stone and others (1997)
10^{-3}	Bakaninbreen, Svalbard (slug tests)	Kulesa and Murray (2003)
$10^{-3} - 10^{-2}$	Haut Glacier d'Arolla, Switzerland (slug tests)	Kulesa and others (2005)
10^{-2}	Gornergletscher, Switzerland (slug tests)	Iken and others (1996)

569 location consisted exclusively of Darcian flow through subglacial sediments with a hydraulic conductivity
 570 $K \leq 10^{-6} \text{ m s}^{-1}$.

571 Borehole drainage at the ice-sediment interface may be physically similar, but of lower magnitude, to that
 572 which occurs during the subglacial drainage of proglacial (Sugiyama and others, 2008) and supraglacial lakes
 573 (Doyle and others, 2013; Dow and others, 2015; Stevens and others, 2015; Tsai and Rice, 2010, 2012; Hewitt
 574 and others, 2018) via a broad, turbulent, and transient sheet. The ephemeral nature of gap opening, which

575 we infer from declining hydraulic transmissivity measurements, supports the hypothesis that gap opening
576 is elastic, which is consistent with the linear elastic rheology of ice over short time scales (Sinha, 1978).
577 Rapid water flow into this narrow gap is likely to be turbulent (Section 3.1.1); however, flow must become
578 laminar near the gap tip as the width of the gap decreases to zero, and flow velocity will also decrease with
579 distance from the injection point (Hewitt and others, 2018). Continued sheet flow through a uniform gap
580 would be unstable as irregularities in flow would theoretically favour the formation of conduits through
581 preferential sediment erosion and concentrated ice melt from frictional heat (Röthlisberger, 1972; Walder
582 and Fowler, 1994; Ng, 2000). Conduit development beneath kilometre-thick ice is, however, anticipated to
583 require continuous water supply at high pressure over prolonged periods, which may only occur if there is
584 continued water input from the surface (e.g. Dow and others, 2014, 2015). Hence, our inference of complete,
585 or at least partial, gap closure in response to declining pressure is consistent with existing theory as the
586 water volumes provided by borehole drainage and subsequent pumping ($\sim 15 \text{ m}^3$) are likely insufficient to
587 establish an efficient conduit beneath kilometre-thick ice. The development of efficient conduits in response
588 to borehole breakthrough can also be excluded by the low discharge rate of $8.4 \times 10^{-5} \text{ m}^3 \text{ s}^{-1}$ calculated
589 from the 45 h required for hydraulic head to recover to the equilibrium level following the injection of
590 13.6 m^3 of water at BH19g breakthrough and during the drill stem raise. Although we cannot rule out the
591 persistence of stable sheet flow following borehole drainage (facilitated by clasts partially supporting the
592 ice overburden pressure (Creys and Schoof, 2009), our observations of a progressive decrease in hydraulic
593 transmissivity can be entirely explained by elastic gap closure and a reversion to Darcian flow through the
594 sediment layer.

595 The instantaneous 0.11 m pressure drop in BH19c in response to BH19g breakthrough (Fig. 4a) provides
596 direct evidence for the hypothesis of Murray and Clarke (1995) that pressure variations can be transmitted
597 to unconnected cavities through elastic displacement of the ice roof. Murray and Clarke (1995) theorised
598 that uplift caused by high water pressure relieves the pressure in adjacent hydraulically-isolated cavities.
599 This hypothesis is one of three hypotheses of mechanical forcing of water pressure that have been proposed
600 to explain the often observed diurnal variation of water pressure in hydrologically-isolated cavities that is
601 out of phase with both ice velocity and water pressure in boreholes and moulins deemed to be connected to
602 efficient subglacial conduits (Murray and Clarke, 1995; Engelhardt and Kamb, 1997; Gordon and others,
603 1998; Dow and others, 2011; Andrews and others, 2014; Ryser and others, 2014; Lefevre and others, 2015;
604 Meierbachtol and others, 2016; Rada and Schoof, 2018). While we cannot rule out the possibility that

605 such anti-correlated diurnal pressure and velocity variations in BH19c (Fig. 8) can be attributed to the
606 alternative hypotheses of cavity expansion and contraction caused by longitudinal strain (Ryser and others,
607 2014) or basal sliding (Iken and Truffer, 1997; Bartholomaus and others, 2011; Hoffman and Price, 2014),
608 displacement of the ice roof due to elastic uplift during gap-opening at BH19g breakthrough can entirely
609 explain the 0.11 m instantaneous pressure drop in BH19c. It is therefore plausible that elastic displacement
610 of the ice roof by diurnal pressure variations within a nearby conduit also explains the anti-correlated
611 diurnal variations in BH19c pressure. This assertion is supported by three-dimensional full-Stokes modelling
612 (Lefeuvre and others, 2018) that reproduced anti-correlated pressure variations between connected and
613 unconnected components of the subglacial drainage system without invoking cavity expansion caused by
614 sliding.

615 Similar to borehole breakthrough events, we argue that water flow at the ice-sediment interface may
616 also occur at times of naturally high subglacial water pressures. The greater variability in meltwater
617 supply means that gap opening at the ice-sediment interface is more likely to occur naturally on the
618 Greenland Ice Sheet and on mountain glaciers than on the West Antarctic ice streams where the process
619 was originally inferred (Engelhardt and Kamb, 1997). Hence, gap opening at the ice-sediment interface
620 has important implications for our understanding of subglacial hydrological systems that extends beyond
621 its ability to explain the drainage of boreholes. Subglacial hydrology in ice sheet models may for instance
622 include exchanges of water flowing partly at the interface and partly within subglacial sediment, which
623 has proven efficient in reproducing day to day variations in ice flow as observed at the land-terminating
624 southwest ice margin (Bougamont and others, 2014). Darcian flow and gap-opening therefore provide a
625 physical explanation for the partitioning of water flowing at the interface and within subglacial sediment.

626 Gap-opening may also play a role in the formation and growth of subglacial drainage systems. Within
627 the framework of existing theory, gap opening provides the initial conduit that may later develop into an
628 inefficient narrow orifice in a distributed (i.e. linked cavity) drainage system (Kamb, 1987), which may
629 ultimately develop into an efficient channel or canal (Röthlisberger, 1972; Walder and Fowler, 1994; Ng,
630 2000). That the overpressure of a water-filled vertical conduit stretching from the surface to the bed (that
631 is, a borehole) can open a gap at the ice-sediment interface, despite the low volumes of water involved,
632 has implications for the establishment of subglacial drainage of the much larger water volumes supplied
633 via moulins, crevasses, and supraglacial lakes. It illustrates the manner in which regions of the basal
634 environment can become hydrologically connected during peaks in water pressure. Gap opening can explain

635 transient periods of borehole water pressure synchronicity that abruptly punctuate the often observed long
636 term pattern of anti-correlated variations in water pressure and velocity measured in hydraulically-isolated
637 cavities during periods of high water pressure (e.g. Murray and Clarke, 1995; Engelhardt and Kamb,
638 1997; Harper and others, 2007; Andrews and others, 2014; Rada and Schoof, 2018). If areas of the bed
639 that were previously hydraulically isolated experience net drainage as a result of gap opening at the ice-
640 sediment interface, it may also explain the hydro-mechanical regulation of ice flow (e.g. Sole and others,
641 2013; Tedstone and others, 2015; Davison and others, 2020), which observations suggest cannot be entirely
642 explained by water pressures within efficient channels (Andrews and others, 2014). It follows that drainage
643 at the ice-sediment interface and Darcian flow through sediments with a low hydraulic conductivity may be
644 two of potentially multiple processes behind the hypothesised weakly-connected component of the subglacial
645 drainage system (Hoffman and others, 2016).

646 A drainage system consisting of cavities, which we assume are present at the base of our boreholes,
647 linked via gaps opened at the ice-sediment interface would at first appear similar to the linked cavity
648 theory of glacial drainage, which consists of cavities connected via narrow orifices (e.g. Kamb, 1987). There
649 is, however, an important distinction in that the linked cavity model specifies that orifices are continuously
650 open and water flow is inefficient and turbulent due to the length and narrowness of orifices (Kamb,
651 1987). Modification of the linked cavity theory to allow transient gap opening between cavities under high
652 water pressure with turbulent flow would explain the same characteristics associated with linked cavity
653 drainage systems: enhanced basal motion, sediment entrainment (as indicated by increased turbidity), and
654 increased connectivity of the bed at times of high water pressure. It would also explain the existence of
655 neighbouring yet behaviourally-independent subglacial drainage subsystems in close proximity (e.g. Murray
656 and Clarke, 1995; Harper and others, 2007; Rada and Schoof, 2018), which the majority of previous models
657 of subglacial drainage cannot reproduce as they inherently allow water to diffuse across the entire glacier
658 bed (e.g. Schoof, 2010; Hewitt, 2013; Werder and others, 2013). This implies a strong link between subglacial
659 hydrology, stresses within the ice, and basal motion that will be challenging to reproduce within numerical
660 models due to the requirement to combine linear-elastic gap opening with a viscous ice rheology.

661 To date, every borehole drilled on Sermeq Kujalleq (Store Glacier) drained rapidly and immediately upon
662 reaching the bed. This includes three boreholes at R30 in 2019, four boreholes at R29 in 2018 (unpublished),
663 and seven boreholes at S30 in 2014 and 2016 (Doyle and others, 2018). A similar pattern of rapid borehole
664 drainage, with a small number of exceptions, has been reported for Whillans Ice Stream in West Antarctica

665 (Engelhardt and Kamb, 1997) and Sermeq Kujalleq (Jakobshavn Isbræ) in West Greenland (Lüthi, 1999).
666 While the results presented here provide further evidence for gap opening as a mechanism for rapid borehole
667 drainage, it also raises the question of why some boreholes on other ice masses don't drain rapidly upon
668 reaching the bed. Some boreholes appear to never drain (e.g. Smart, 1996), while others drain slowly
669 (e.g. Andrews and others, 2014), and others drain after a delay (e.g. Gordon and others, 2001; Kamb and
670 Engelhardt, 1987; Engelhardt and Kamb, 1997; Fischer and Clarke, 2001). This heterogeneity, which often
671 occurs within the same field site, could be explained by the stress regime, boreholes terminating blind in
672 debris-rich basal ice before they are able to connect to the subglacial drainage system, or by the presence
673 of impermeable barriers such as areas of ice-bedrock contact or cold ice, the latter of which can occur
674 even within predominantly temperate glaciers (Robin, 1976). A detailed discussion of the heterogeneity of
675 borehole drainage is not warranted here (see instead Smart, 1996; Gordon and others, 2001), but we do
676 seek an explanation for the homogeneity in borehole drainage observed to date on Sermeq Kujalleq (Store
677 Glacier). Hot water drilling is ineffective at penetrating debris-rich basal ice, which is characteristic of many
678 exposed margins of the Greenland Ice Sheet, for example on Russell Glacier (Knight and others, 2002) and
679 at the base of icebergs discharging from Sermeq Kujalleq (Jakobshavn Isbræ; Lüthi and others, 2009), yet
680 none of the boreholes drilled to date on Sermeq Kujalleq (Store Glacier) terminated above the bed due
681 to an obstruction by englacial clasts. We therefore speculate (while noting the small number of boreholes
682 drilled at a limited number of sites) that debris content within basal ice on Sermeq Kujalleq (Store Glacier)
683 may be low. If so, this could be explained by the removal of debris-rich basal ice formed upstream by basal
684 melt. Furthermore, low (and potentially even negative) effective pressures (e.g. -46 ± 102 kPa at R30;
685 Table 1) are conducive to hydraulic ice-bed separation (e.g. Schoof and others, 2012) and these conditions
686 are found at all the Sermeq Kujalleq (Store Glacier) sites drilled to date. Modelling of subglacial drainage
687 through a poroelastic sediment and cavity beneath ice suggests that elastic gap opening is enabled by the
688 suction of water from an underlying porous sediment layer without the requirement for a pre-wetted water
689 film (Hewitt and others, 2018). We therefore conclude that rapid borehole drainage on Sermeq Kujalleq
690 (Store Glacier) is facilitated by low effective pressures, subglacial sediment, and a potentially low debris
691 content within basal ice.

692 Booth and others (2020) used the low basal reflectivity in vertical seismic profiles to infer that the
693 subglacial sediment layer at site R30 has an acoustic impedance similar to that of basal ice, and from this,
694 they suggested that the sediment is consolidated, and neither deforming nor lithified. The inference that

695 the sediment layer is not deforming implies that the fast ice velocity at this site must be accommodated
696 by either enhanced internal deformation of the ice, ice-sediment decoupling under high water pressure (e.g.
697 Iverson and others, 1995), or deformation of a sediment layer thinner than the 10 m vertical resolution of the
698 seismic technique. With regard to the last assertion we note that sediment deformation often occurs within
699 an upper layer that is typically only decimetres to a few metres thick (e.g. Clarke, 1987; Murray, 1997;
700 Humphrey and others, 1993; Engelhardt and Kamb, 1998), and that the shape of the pressure pulse during
701 BH19g breakthrough can only be reproduced using the model of Hewitt and others (2018) if the sediment
702 layer is deformable. While the extent of sediment deformation beneath this site remains inconclusive the
703 evidence presented herein supports the hypothesis of ice-sediment decoupling under periods of high water
704 pressure. Indeed, we suggest that the theory of gap opening at the ice-sediment interface (Engelhardt and
705 Kamb, 1997) may involve the same physical process as ice-sediment decoupling envisaged by Iverson and
706 others (1995). To explain the reverse tilt of inclinometers just below the ice-sediment interface, Iverson
707 and others (1995) envisaged that sediment would be squeezed into the zone of uplift at times of high water
708 pressure. Further evidence for gap opening and decoupling at the ice-sediment interface is provided by
709 (as far as we are aware) unrepeated, direct observation of a cm-wide gap at the ice-sediment interface of
710 Blue Glacier, USA (Engelhardt and others, 1978). Borehole photography revealed a ~ 0.1 m thick sediment
711 layer overlying bedrock that was mechanically and visibly distinct from a 0.1 – 16.0 m thick debris-laden
712 basal ice layer. Engelhardt and others (1978) suggested that the gap was opened by the overpressure of
713 the water-filled borehole and that basal sliding velocities were faster where gaps were present. They also
714 inferred that interstitial pressure within the sediment must be close to or at the ice overburden pressure in
715 order to prevent the basal ice merging with the sediment layer through regelation, an assertion supported
716 by Rempel (2008). Hence, further in situ observations are required to investigate whether ice-sediment
717 decoupling occurs via a gap at the ice-sediment interface or through an increase in the thickness of the
718 sediment layer as proposed by Iverson and others (1995), or a combination of both processes as modelled
719 by Hewitt and others (2018).

720 5. CONCLUSIONS

721 Detailed measurements of pressure pulses during a borehole breakthrough event, and a decrease in hydraulic
722 transmissivity with time since breakthrough, provide evidence for hydraulic gap opening and closure at the
723 ice-sediment interface, with gaps opening and closing elastically in response to water pressure. Analysis
724 of the subsequent recovery of subglacial water pressure indicates that the hydraulic conductivity of the

725 subglacial sediment layer is on the order of $10^{-7} - 10^{-6} \text{ m s}^{-1}$, which suggests it is coarse-grained and
726 more permeable than the fine-grained sediments beneath West Antarctic ice streams. As seismic surveys
727 suggest that sediment at this site is consolidated, we infer that fast basal motion may be accommodated
728 by ice-sediment decoupling and potentially shallow-depth sediment deformation in a layer thinner than the
729 10 m resolution of the seismic technique.

730 Observations of a pressure drop simultaneous with the breakthrough of a borehole 70 m away provides
731 direct evidence for the hypothesis that anti-correlations between water pressure in connected and
732 unconnected regions of the bed can be explained via elastic displacement of the ice roof.

733 We argue that water flow via gaps opened at the ice-sediment interface is likely to play a critical role in
734 both basal motion and the development of subglacial hydrology on soft-bedded ice masses, and that Darcian
735 flow through sediments may explain the drainage and recharge of areas of the bed that are otherwise
736 hydrologically isolated.

737 ACKNOWLEDGEMENTS

738 This research was funded by the European Research Council as part of the RESPONDER project under
739 the European Union's Horizon 2020 research and innovation program (Grant 683043). T.R.C. and R.L.
740 were supported by Natural Environment Research Council Doctoral Training Partnership Studentships
741 (Grant NE/L002507/1). We thank Lee Greenler for providing the code for modelling borehole diameter;
742 Katie Miles, Emma Docherty and Tom Chase for assistance in the construction of borehole sensor strings;
743 and Sean Peters, Mickey MacKie, Mike Prior-Jones, Eliza Dawson and Tun Jan Young for assistance in the
744 field. We are very grateful to Ann Andreasen and the Uummannaq Polar Institute for their kind hospitality.

745 SUPPLEMENTARY MATERIAL

746 The supplementary material is provided as a separate document and includes two supplementary tables
747 and four supplementary figures.

748 DATASET AVAILABILITY

749 The datasets presented in this paper will be made available in a repository prior to final publication.

750 **AUTHOR CONTRIBUTION STATEMENT**

751 The overall research project (RESPONDER) was led by PC, with BH leading the hot water drilling and
752 borehole instrumentation reported herein. Data collection was led by SD, with contributions from BH, PC,
753 RL, CS and TC. SD conducted the data analysis. RL adapted and ran the borehole drilling model. TC
754 surveyed the borehole positions and led site mapping. DH and JN calculated the breakthrough volumetric
755 flux and pressure response. The manuscript was written by SD, with contributions from all co-authors.

756 **REFERENCES**

- 757 Alley R, Blankenship D, Bentley C, and Rooney S (1986) Deformation of till beneath Ice Stream B, West Antarctica.
758 *Nature*, **322**, 57–59 (doi: 10.1038/322057a0.)
- 759 Alley R, Blankenship D, Rooney S and Bentley C (1989) Water-pressure coupling of sliding and bed
760 deformation: III. Application to Ice Stream B, Antarctica. *Journal of Glaciology*, **35**(119), 130–139 (doi:
761 10.3189/002214389793701572)
- 762 Alley RB, Cuffey KM and Zoet LK (2019) Glacial erosion: status and outlook. *Annals of Glaciology*, **60**(80), 1–13
763 (doi: 10.1017/aog.2019.38)
- 764 Andrews LC, Catania GA, Hoffman MJ, Gulley JD, Lüthi MP, Ryser C, Hawley RL and Neumann TA (2014) Direct
765 observations of evolving subglacial drainage beneath the Greenland Ice Sheet. *Nature*, **514**(7520), 80–83 (doi:
766 10.1038/nature13796)
- 767 Bartholomaus T, Anderson R and Anderson S (2011) Growth and collapse of the distributed subglacial hydrologic
768 system of Kennicott Glacier, Alaska, USA, and its effects on basal motion. *Journal of Glaciology*, **57**(206), 985–1002
769 (doi: 10.3189/002214311798843269)
- 770 Blankenship DD, Bentley CR, Rooney ST and Alley RB (1986) Seismic measurements reveal a saturated porous
771 layer beneath an active Antarctic ice stream. *Nature*, **322**(6074), 54–57 (doi: 10.1038/322054a0)
- 772 Booth AD, Christoffersen P, Schoonman C, Clarke A, Hubbard B, Law R, Doyle SH, Chudley TR and Chalari A
773 (2020) Distributed acoustic sensing of seismic properties in a borehole drilled on a fast-flowing Greenlandic outlet
774 glacier. *Geophysical Research Letters*, **47**(13), e2020GL088148 (doi: 10.1029/2020GL088148)
- 775 Bougamont M, Christoffersen P, Hubbard A, Fitzpatrick A, Doyle S and Carter S (2014) Sensitive response
776 of the Greenland Ice Sheet to surface melt drainage over a soft bed. *Nature Communications*, **5**, 5052 (doi:
777 10.1038/ncomms6052)
- 778 Boulton GS and Dent D (1974) The nature and rates of post-depositional changes in recently deposited
779 till from south-east Iceland. *Geografiska Annaler: Series A, Physical Geography*, **56**(3-4), 121–134 (doi:
780 10.1080/04353676.1974.11879894)

- 781 Christianson K, Peters L, Alley R, Anandakrishnan S, Jacobel R, Riverman K, Muto A and Keisling B (2014) Dilatant
782 till facilitates ice-stream flow in northeast Greenland. *Earth and Planetary Science Letters*, **401**(0), 57–69 (doi:
783 10.1016/j.epsl.2014.05.060)
- 784 Chudley TR, Christoffersen P, Doyle SH, Abellan A and Snooke N (2019a) High-accuracy UAV photogrammetry of
785 ice sheet dynamics with no ground control. *The Cryosphere*, **13**(3), 955–968 (doi: 10.5194/tc-13-955-2019)
- 786 Chudley TR, Christoffersen P, Doyle SH, Bougamont M, Schoonman CM, Hubbard B and James MR (2019b)
787 Supraglacial lake drainage at a fast-flowing Greenlandic outlet glacier. *Proceedings of the National Academy of*
788 *Sciences* (doi: 10.1073/pnas.1913685116)
- 789 Clarke GKC (1987) Subglacial till: A physical framework for its properties and processes. *Journal of Geophysical*
790 *Research: Solid Earth*, **92**(B9), 9023–9036 (doi: 10.1029/JB092iB09p09023)
- 791 Cooper H and Jacob C (1946) A generalized graphical method for evaluating formation constants and summarizing
792 well field history. *American Geophysical Union Transactions*, **27**, 526–534 (doi: 10.1029/TR027i004p00526)
- 793 Creyts TT and Schoof CG (2009) Drainage through subglacial water sheets. *Journal of Geophysical Research: Earth*
794 *Surface*, **114**(F4), ISSN 2156-2202 (doi: 10.1029/2008JF001215), f04008
- 795 Davison BJ, Sole AJ, Cowton TR, Lea JM, Slater DA, Fahrner D and Nienow PW (2020) Subglacial drainage
796 evolution modulates seasonal ice flow variability of three tidewater glaciers in southwest Greenland. *Journal of*
797 *Geophysical Research: Earth Surface*, **125**(9), e2019JF005492 (doi: 10.1029/2019JF005492)
- 798 de Marsily G (1986) *Quantitative Hydrogeology*. Academic Press Inc., Orlando, Florida
- 799 Dow C, Kavanaugh J, Sanders J, Cuffey K and MacGregor K (2011) Subsurface hydrology of an overdeepened cirque
800 glacier. *Journal of Glaciology*, **57**(206), 1067–1078 (doi: 10.3189/002214311798843412)
- 801 Dow C, Kulesa B, Rutt I, Doyle H S and Hubbard A (2014) Upper bounds on subglacial channel
802 development for interior regions of the Greenland ice sheet. *Journal of Glaciology*, **60**(224), 1044–1052 (doi:
803 10.3189/2014JoG14J093)
- 804 Dow CF, Kulesa B, Rutt IC, Tsai VC, Pimentel S, Doyle S, van As D, Lindbäck K K, Pettersson R, Jones GA and
805 Hubbard A (2015) Modeling of subglacial hydrological development following rapid supraglacial lake drainage.
806 *Journal of Geophysical Research: Earth Surface* (doi: 10.1002/2014JF003333)
- 807 Doyle S, Hubbard A, Dow C, Jones G, Fitzpatrick A, Gusmeroli A, Kulesa B, Lindback K, Pettersson R and Box
808 J (2013) Ice tectonic deformation during the rapid in situ drainage of a supraglacial lake on the Greenland Ice
809 Sheet. *The Cryosphere*, **7**(1), 129–140 (doi: 10.5194/tc-7-129-2013)
- 810 Doyle SH, Hubbard B, Christoffersen P, Young TJ, Hofstede C, Bougamont M, Box JE and Hubbard A (2018)
811 Physical conditions of fast glacier flow: 1. Measurements from boreholes drilled to the bed of Store Glacier, West
812 Greenland. *Journal of Geophysical Research: Earth Surface*, **123**(2), 324–348 (doi: 10.1002/2017JF004529)

- 813 Engelhardt H (1978) Water in glaciers: observations and theory of the behaviour of water levels in boreholes. *Z.*
814 *Gletscher. Glazialgeol.*, **14**, 35–60
- 815 Engelhardt H and Kamb B (1997) Basal hydraulic system of a West Antarctic ice stream: constraints from borehole
816 observations. *Journal of Glaciology*, **43**(144), 207–229 (doi: 10.3198/1997JoG43-144-207-230)
- 817 Engelhardt H and Kamb B (1998) Basal sliding of Ice Stream B, West Antarctica. *Journal of Glaciology*, **44**(147),
818 223–230 (doi: 10.3189/S0022143000002562)
- 819 Engelhardt H, Humphrey N, Kamb B and Fahnestock M (1990) Physical conditions at the base of a fast moving
820 Antarctic ice stream. *Science*, **248**(4951), 57–59 (doi: 10.1126/science.248.4951.57)
- 821 Engelhardt HF, Harrison WD and Kamb B (1978) Basal sliding and conditions at the glacier bed as revealed by
822 borehole photography. *Journal of Glaciology*, **20**(84), 469–508 (doi: 10.3198/1978JoG20-84-469-508)
- 823 Fischer UH and Clarke GK (2001) Review of subglacial hydro-mechanical coupling: Trapridge Glacier, Yukon
824 Territory, Canada. *Quaternary International*, **86**(1), 29–43 (doi: 10.1016/S1040-6182(01)00049-0)
- 825 Fischer UH, Iverson NR, Hanson B, LeB Hooke R and Jansson P (1998) Estimation of hydraulic prop-
826 erties of subglacial till from ploughmeter measurements. *Journal of Glaciology*, **44**(148), 517–522 (doi:
827 10.3189/S0022143000002033)
- 828 Flowers G and Clarke G (2002) A multicomponent coupled model of glacier hydrology 1. Theory and synthetic
829 examples. *Journal of Geophysical Research*, **107**,(B11) (doi: 10.1029/2001JB001122,)
- 830 Fountain A (1994) Borehole water-level variations and implications for the subglacial hydraulics of South Cascade
831 Glacier, Washington State, USA. *Journal of Glaciology*, **40**(135), 293–304 (doi: 10.3189/S0022143000007383)
- 832 Freeze RA and Cherry JA (1979) *Groundwater*. Prentice-Hall Inc., Englewood Cliffs, N.J.
- 833 Gordon S, Sharp M, Hubbard B, Smart C, Ketterling B and Willis I (1998) Seasonal reorganization of subglacial
834 drainage system of Haut Glacier d’Arolla, Valais, Switzerland, inferred from measurements in boreholes.
835 *Hydrological Processes*, **12**, 105–133
- 836 Gordon S, Sharp M, Hubbard B, Willis I, Smart C, Copland L, Harbor J and Ketterling B (2001) Borehole drainage
837 and its implications for the investigation of glacier hydrology: experiences from Haut Glacier d’Arolla, Switzerland.
838 *Hydrological Processes*, **15**, 797–813 (doi: 10.1002/hyp.184)
- 839 Greenler L, Benson T, Cherwinka J, Elcheikh A, Feyzi F, Karle A and Paulos R (2014) Modeling hole size, lifetime and
840 fuel consumption in hot-water ice drilling. *Annals of Glaciology*, **55**(68), 115–123 (doi: 10.3189/2014AoG68A033)
- 841 Haldorsen S and Krüger J (1990) Till genesis and hydrogeological properties. *Hydrology Research*, **21**(2), 81–94 (doi:
842 10.2166/nh.1990.0006)
- 843 Harper J, Humphrey N, Pfeffer W and Lazar B (2007) Two modes of accelerated glacier sliding related to water.
844 *Geophysical Research Letters*, **34**, L12503 (doi: 10.1029/2007GL030233)

- 845 Hewitt DR, Chini GP and Neufeld JA (2018) The influence of a poroelastic till on rapid subglacial flooding and
846 cavity formation. *Journal of Fluid Mechanics*, **855**, 1170–1207 (doi: 10.1017/jfm.2018.624)
- 847 Hewitt I (2013) Seasonal changes in ice sheet motion due to melt water lubrication. *Earth and Planetary Science
848 Letters*, **371–372**, 16–25 (doi: 10.1016/j.epsl.2013.04.022)
- 849 Hiscock K and Bense V (2014) *Hydrogeology: Principles and Practice*. Wiley-Blackwell, 2nd edition
- 850 Hodge SM (1979) Direct measurement of basal water pressures: Progress and problems. *Journal of Glaciology*, **23**(89),
851 309–319 (doi: 10.3189/S0022143000029920)
- 852 Hoffman M and Price S (2014) Feedbacks between coupled subglacial hydrology and glacier dynamics. *Journal of
853 Geophysical Research: Earth Surface*, **119**(3), 414–436 (doi: 10.1002/2013JF002943)
- 854 Hoffman MJ, Andrews LC, Price SA, Catania GA, Neumann TA, Lüthi MP, Gulley J, Ryser C, Hawley RL and
855 Morriss B (2016) Greenland subglacial drainage evolution regulated by weakly connected regions of the bed. *Nature
856 Communications*, **7** (doi: 10.1038/ncomms13903)
- 857 Hofstede C, Christoffersen P, Hubbard B, Doyle SH, Young TJ, Diez A, Eisen O and Hubbard A (2018) Physical
858 conditions of fast glacier flow: 2. Variable extent of anisotropic ice and soft basal sediment from seismic reflection
859 data acquired on Store Glacier, West Greenland. *Journal of Geophysical Research: Earth Surface*, **123**(2), 349–362
860 (doi: 10.1002/2017JF004297)
- 861 Hubbard B and Maltman A (2000) Laboratory investigations of the strength, static hydraulic conductivity
862 and dynamic hydraulic conductivity of glacial sediments, In: Maltman, A., Hubbard, B., and Hambrey, M.J.
863 *Deformation of Glacial Materials*, **176**, 231–242
- 864 Hubbard B, Sharp M, Willis I, Nielsen M and Smart C (1995) Borehole water-level variations and the structure of
865 the subglacial hydrological system of Haut Glacier d’Arolla, Valais, Switzerland. *Journal of Glaciology*, **41**(139),
866 572–583 (doi: 10.3189/S0022143000034894)
- 867 Hubbard B, Christoffersen P, Doyle SH, Chudley TR, Schoonman CM, Law R and Bougamont M (2021) Borehole-
868 based characterization of deep mixed-mode crevasses at a greenlandic outlet glacier. *AGU Advances*, **2**(2),
869 e2020AV000291 (doi: <https://doi.org/10.1029/2020AV000291>), e2020AV000291 2020AV000291
- 870 Humphrey N, Kamb B, Fahnestock M and Engelhardt H (1993) Characteristics of the bed of the lower Columbia
871 Glacier, Alaska. *Journal of Geophysical Research: Solid Earth*, **98**(B1), 837–846 (doi: 10.3189/002214390793701354)
- 872 Iken A and Bindshadler R (1986) Combined measurements of subglacial water pressure and surface velocity of
873 Findelgletscher, Switzerland: conclusions about drainage system and sliding mechanisms. *Journal of Glaciology*,
874 **32**(110), 101–119 (doi: 10.3189/S0022143000006936)
- 875 Iken A and Truffer M (1997) The relationship between subglacial water pressure and velocity of Find-
876 elgletscher, Switzerland, during its advance and retreat. *Journal of Glaciology*, **43**(144), 328–338 (doi:
877 10.3189/S0022143000003282)

- 878 Iken A, Fabri K and Funk M (1996) Water storage and subglacial drainage conditions inferred from
879 borehole measurements on Gornergletscher, Valais, Switzerland. *Journal of Glaciology*, **42**(141), 233–248 (doi:
880 10.3189/S0022143000004093)
- 881 Iverson N, Hanson B, Hooke RL and Jansson P (1995) Flow mechanism of glaciers on soft beds. *Science*, **267**(5194),
882 80–81 (doi: 10.1126/science.267.5194.80)
- 883 Iverson NR, Jansson P and Hooke RL (1994) In-situ measurement of the strength of deforming subglacial till. *Journal*
884 *of Glaciology*, **40**(136), 497–503 (doi: 10.3189/S0022143000012375)
- 885 Kamb B (1987) Glacier surge mechanism based on linked-cavity configuration of the basal water conduit system.
886 *Journal of Geophysical Research*, **92**(B9), 9083–9100 (doi: 10.1029/JB092iB09p09083)
- 887 Kamb B (2001) *Basal zone of the West Antarctic ice streams and its role in lubrication of their rapid motion:*
888 *In: The West Antarctic Ice Sheet: Behavior and Environment*, 157–199. American Geophysical Union (doi:
889 <https://doi.org/10.1029/AR077p0157>)
- 890 Kamb B and Engelhardt H (1987) Waves of accelerated motion in a glacier approaching surge: the mini-surges of
891 Varigated Glacier, Alaska, U.S.A. *Journal of Glaciology*, **33**(113), 27–46 (doi: 10.3189/S0022143000005311)
- 892 Knight PG, Waller RI, Patterson CJ, Jones AP and Robinson ZP (2002) Discharge of debris from ice at the margin
893 of the Greenland ice sheet. *Journal of Glaciology*, **48**(161), 192–198 (doi: 10.3189/172756502781831359)
- 894 Kulesa B and Hubbard B (1997) Interpretation of borehole impulse tests at Haut Glacier d’Arolla, Switzerland.
895 *Annals of Glaciology*, **24**, 397–402 (doi: 10.3189/S0260305500012507)
- 896 Kulesa B and Murray T (2003) Slug-test derived differences in bed hydraulic properties between a surge-type and
897 a non-surge-type Svalbard glacier. *Annals of Glaciology*, **36**, 103–109 (doi: 10.3189/172756403781816257)
- 898 Kulesa B, Hubbard B, Williamson M and Brown GH (2005) Hydrogeological analysis of slug tests in glacier boreholes.
899 *Journal of Glaciology*, **51**(173), 269–280 (doi: 10.3189/172756505781829458)
- 900 Law R, Christoffersen P, Hubbard B, Doyle SH, Chudley TR, Schoonman CM, Bougamont M, des Tombe
901 B, Schilperoort B, Kechavarzi C, Booth A and Young TJ (2021) Thermodynamics of a fast-moving
902 greenlandic outlet glacier revealed by fiber-optic distributed temperature sensing. *Science Advances*, **7**(20) (doi:
903 10.1126/sciadv.abe7136)
- 904 Lefevre PM, Jackson M, Lappegard G and Hagen JO (2015) Interannual variability of glacier basal pressure from
905 a 20 year record. *Annals of Glaciology*, **56**(70), 33–44 (doi: 10.3189/2015AoG70A019)
- 906 Lefevre PM, Zwinger T, Jackson M, Gagliardini O, Lappegard G and Hagen JO (2018) Stress redistribution explains
907 anti-correlated subglacial pressure variations. *Frontiers in Earth Science*, **5**, 110 (doi: 10.3389/feart.2017.00110)
- 908 Lingle CS and Brown TJ (1987) A subglacial aquifer bed model and water pressure dependent basal sliding
909 relationship for a West Antarctic ice stream. In CJ Van der Veen and J Oerlemans (eds.), *Dynamics of the*
910 *West Antarctic Ice Sheet*, 249–285, Springer Netherlands, Dordrecht

- 911 Lüthi M (1999) *Experimental and numerical investigation of a firn covered cold glacier and a polythermal ice stream: case studies at Colle Gniffetti and Jakobshavn Isbræ*. Ph.D. thesis, Swiss Federal Institute of Technology Zurich
- 912
- 913 Lüthi M, Fahnestock M and Truffer M (2009) Calving icebergs indicate a thick layer of temperate ice at the base of Jakobshavn Isbræ, Greenland. *Journal of Glaciology*, **55**(191), 563–566 (doi: 10.3189/002214309788816650)
- 914
- 915 Meierbachtol T, Harper J, Humphrey N and Wright P (2016) Mechanical forcing of water pressure in a hydraulically isolated reach beneath Western Greenland's ablation zone. *Annals of Glaciology*, **52**(72), 62–70
- 916
- 917 (doi: 10.1017/aog.2016.5)
- 918 Murray T (1997) Assessing the paradigm shift: Deformable glacier beds. *Quaternary Science Reviews*, **16**(9), 995 –
- 919 1016, ISSN 0277-3791 (doi: 10.1016/S0277-3791(97)00030-9)
- 920 Murray T and Clarke G (1995) Black-box modelling of the subglacial water system. *Journal of Geophysical Research*,
- 921 **100**, 10231–10245 (doi: 10.1029/95JB00671)
- 922 Ng F (2000) Canals under sediment-based ice sheets. *Annals of Glaciology*, **30**(1), 146–152 (doi: 10.3189/172756400781820633)
- 923
- 924 Ó'Cofaigh C, Andrews JT, Jennings AE, Dowdeswell JA, Hogan KA, Kilfeather AA and Sheldon C (2013) Glacimarine lithofacies, provenance and depositional processes on a West Greenland trough-mouth fan. *Journal of Quaternary Science*, **28**(1), 13–26 (doi: 10.1002/jqs.2569)
- 925
- 926
- 927 Porter C, Morin P, Howat I, Noh MJ, Bates B, Peterman K, Keesey S, Schlenk M, Gardiner J, Tomko K, Willis M, Kelleher C, Cloutier M, Husby E, Foga S, Nakamura H, Platson M, Wethington Michael J, Williamson C, Bauer G, Enos J, Arnold G, Kramer W, Becker P, Doshi A, D'Souza C, Cummens F P Laurier and Bojesen M (2018) ArcticDEM, Harvard Dataverse, V1 (doi: 10.7910/DVN/OHHUKH)
- 928
- 929
- 930
- 931 Rada C and Schoof C (2018) Channelized, distributed, and disconnected: Subglacial drainage under a valley glacier in the Yukon. *The Cryosphere*, **12**, 2609–2636 (doi: 10.5194/tc-12-2609-2018)
- 932
- 933 Rempel AW (2008) A theory for ice-till interactions and sediment entrainment beneath glaciers. *Journal of Geophysical Research: Earth Surface*, **113**(F1) (doi: 10.1029/2007JF000870)
- 934
- 935 Rignot E, Box JE, Burgess E and Hanna E (2008) Mass balance of the Greenland ice sheet from 1958 to 2007. *Geophysical Research Letters*, **35**(20), ISSN 1944-8007 (doi: 10.1029/2008GL035417)
- 936
- 937 Robin Gd (1976) Is the basal ice of a temperate glacier at the pressure melting point? *Journal of Glaciology*, **16**(74),
- 938 183–196 (doi: 10.3189/S002214300003152X)
- 939 Ronayne MJ, Houghton TB and Stednick JD (2012) Field characterization of hydraulic conductivity in a heterogeneous alpine glacial till. *Journal of Hydrology*, **458–459**, 103–109, ISSN 0022-1694 (doi: https://doi.org/10.1016/j.jhydrol.2012.06.036)
- 940
- 941
- 942 Röthlisberger H (1972) Water pressure in intra- and subglacial channels. *Journal of Glaciology*, **11**(62), 177–203 (doi: 10.3189/S0022143000022188)
- 943

- 944 Ryser C, Lüthi M, Andrews L, Catania G, Funk M, Hawley R, Hoffman M and Neumann T (2014) Caterpillar-like ice
945 motion in the ablation zone of the Greenland ice sheet. *Journal of Geophysical Research: Earth Surface*, **119**(10),
946 2258–2271
- 947 Schoof C (2010) Ice-sheet acceleration driven by melt water supply variability. *Nature*, **468**, 803–806 (doi:
948 10.1038/nature09618)
- 949 Schoof C, Hewitt IJ and Werder MA (2012) Flotation and free surface flow in a model for subglacial drainage. Part
950 1. Distributed drainage. *Journal of Fluid Mechanics*, **702**, 126 (doi: 10.1017/jfm.2012.165)
- 951 Sinha NK (1978) Short-term rheology of polycrystalline ice. *Journal of Glaciology*, **21**(85), 457–474 (doi:
952 10.3189/S002214300003361X)
- 953 Smart CC (1996) Statistical evaluation of glacier boreholes as indicators of basal drainage systems. *Hydrological*
954 *Processes*, **10**(4), 599–613 (doi: 10.1002/(SICI)1099-1085(199604)10:4<599::AID-HYP394>3.0.CO;2-8)
- 955 Sole A, Nienow P, Bartholomew I, Mair D, Cowton T, Tedstone A and King M (2013) Winter motion mediates
956 dynamic response of the Greenland Ice Sheet to warmer summers. *Geophysical Research Letters*, **40**, 3940–3944
957 (doi: 10.1002/grl.507764)
- 958 Stevens LA, Behn MD, McGuire JJ, Das SB, Joughin I, Herring T, Shean DE and King MA (2015) Greenland
959 supraglacial lake drainages triggered by hydrologically induced basal slip. *Nature*, **522**(7554), 73–76 (doi:
960 10.1038/nature14480)
- 961 Stone D and Clarke G (1993) Estimation of subglacial hydraulic properties from induced changes in basal water
962 pressure: a theoretical framework for borehole-response tests. *Journal of Glaciology*, **39**(132), 327–340 (doi:
963 10.3189/S0022143000015999)
- 964 Stone DB, Clarke GKC and Ellis RG (1997) Inversion of borehole-response test data for estimation of subglacial
965 hydraulic properties. *Journal of Glaciology*, **43**(143), 103–113 (doi: 10.3189/S0022143000002860)
- 966 Sugiyama S, Bauder A, Huss M, Riesen P and Funk M (2008) Triggering and drainage mechanisms of the 2004
967 glacier-dammed lake outburst in Gornergletscher, Switzerland. *Journal of Geophysical Research*, **113**, F04019
968 (doi: 10.1029/2007JF000920)
- 969 Tedstone AJ, Nienow PW, Gourmelen N, Dehecq A, Goldberg D and Hanna E (2015) Decadal slowdown of
970 a land-terminating sector of the Greenland Ice Sheet despite warming. *Nature*, **526**(7575), 692–695 (doi:
971 10.1038/nature15722)
- 972 Theis CV (1935) The relation between the lowering of the piezometric surface and the rate and duration of discharge
973 of a well using ground-water storage. *Eos, Transactions American Geophysical Union*, **16**(2), 519–524 (doi:
974 10.1029/TR016i002p00519)
- 975 Thiem G (1906) *Hydrologische Methoden*. Leipzig, Germany, Gebhardt

- 976 Tsai V and Rice J (2010) A model for turbulent hydraulic fracture and application to crack propagation at glacier
977 beds. *Journal of Geophysical Research*, **115**, F03007 (doi: 10.1029/2009JF001474)
- 978 Tsai VC and Rice JR (2012) Modeling turbulent hydraulic fracture near a free surface. *Journal of Applied Mechanics*,
979 **79**(3), ISSN 0021-8936 (doi: 10.1115/1.4005879), 031003
- 980 Tulaczyk S, Kamb WB and Engelhardt HF (2000) Basal mechanics of Ice Stream B, West Antarctica: 1. Till
981 mechanics. *Journal of Geophysical Research: Solid Earth*, **105**(B1), 463–481 (doi: 10.1029/1999JB900329)
- 982 Waddington BS and Clarke GK (1995) Hydraulic properties of subglacial sediment determined from the mechanical
983 response of water-filled boreholes. *Journal of Glaciology*, **41**(137), 112–124 (doi: 10.3189/S0022143000017810)
- 984 Walder J and Fowler A (1994) Channelized subglacial drainage over a deformable bed. *Journal of Glaciology*, **40**(134),
985 3–15 (doi: 10.3189/S0022143000003750)
- 986 Walter F, Chaput J and Luthi M (2014) Thick sediments beneath Greenland's ablation zone and their potential role
987 in future ice sheet dynamics. *Geology*, **42**(6), 487–490 (doi: 10.1130/G35492.1)
- 988 Weertman J (1970) A method for setting a lower limit on the water layer thickness at the bottom of an ice sheet
989 from the time required for upwelling of water into a borehole. *IAHS Publ.*, **86**, 69–73
- 990 Weertman J (1972) General theory of water flow at the base of a glacier or ice sheet. *Reviews of Geophysics*, **10**(1),
991 287–333 (doi: 10.1029/RG010i001p00287)
- 992 Werder MA, Hewitt IJ, Schoof CG and Flowers GE (2013) Modeling channelized and distributed subglacial drainage
993 in two dimensions. *Journal of Geophysical Research: Earth Surface*, **118**(4), 2140–2158 (doi: 10.1002/jgrf.20146)
- 994 Young TJ, Christoffersen P, Doyle SH, Nicholls KW, Stewart CL, Hubbard B, Hubbard A, Lok LB, Brennan PV,
995 Benn DI, Luckman A and Bougamont M (2019) Physical conditions of fast glacier flow: 3. Seasonally-evolving ice
996 deformation on Store Glacier, West Greenland. *Journal of Geophysical Research: Earth Surface*, **124**(1), 245–267
997 (doi: 10.1029/2018JF004821)

998 APPENDIX A. TRANSMISSIVITY FROM TIME CONSTANT

The hydraulic transmissivity (T_g) of a porous medium equivalent to a gap of uniform width δ is given by de Marsily (1986) as

$$T_g = \frac{\phi \delta^3 \rho_w g}{12 \mu_w}. \quad (\text{A1})$$

The time constant D is given by

$$D = \frac{6 \mu_w r_s^2}{\delta^3 \rho_w g} \ln \frac{R}{r_0}, \quad (\text{A2})$$

which is Equation 7a of Weertman (1970) and Equation 9 of Engelhardt and Kamb (1997). Combining Equations A1 and A2 as follows allows the hydraulic transmissivity to be approximated from the time constant D . Inserting ϕ and then multiplying both sides of Equation A2 by two gives

$$2D = \frac{12\mu_w r_s^2}{\phi \delta^3 \rho_w g} \ln \frac{R}{r_0}. \quad (\text{A3})$$

This permits simplification by inserting the inverse of Equation A1 into Equation A3

$$2D = \frac{1}{T_g} r_s^2 \ln \frac{R}{r_0}. \quad (\text{A4})$$

Multiplying both sides by T gives

$$2DT_g = r_s^2 \ln \frac{R}{r_0}. \quad (\text{A5})$$

And further rearranging gives

$$T_g = \frac{r_s^2}{2D} \ln \frac{R}{r_0}, \quad (\text{A6})$$

999 which is Equation 8.7 of Lüthi (1999) and Equation 26 of this paper.

1000 APPENDIX B. BOREHOLE RADIUS

As the hose radius (r_d) and speed (U_d) are known, the differential rate of change in hydraulic head below and above the water line during the BH19g(e) pumping test allows the borehole radius at the water line (r_s) to be determined as follows. The total volumetric flux of water stored within the borehole when the drill hose was below the water line during PT2 is $Q_{b2} = Q_{s2} + Q_{d2}$, or alternatively

$$Q_{b2} = (\pi r_s^2 - \pi r_d^2) \frac{dh_2}{dt} + \pi r_d^2 U_d, \quad (\text{B1})$$

where the numeric subscript indicates the period. Similarly the borehole storage flux with the drill stem above the water line during PT3 is

$$Q_{b3} = \pi r_s^2 \frac{dh_3}{dt}. \quad (\text{B2})$$

Assuming water input (Q_i) and output (Q_o) were constant at the transition from PT2 to PT3

$$Q_{b2} = Q_{b3}. \quad (\text{B3})$$

Therefore equating fluxes gives

$$(\pi r_s^2 - \pi r_d^2) \frac{dh_2}{dt} + \pi r_d^2 U_d = \pi r_s^2 \frac{dh_3}{dt}. \quad (\text{B4})$$

Expanding on the left hand side gives

$$\pi r_s^2 \frac{dh_2}{dt} - \pi r_d^2 \frac{dh_2}{dt} + \pi r_d^2 U_d = \pi r_s^2 \frac{dh_3}{dt}. \quad (\text{B5})$$

Rearranging gives

$$\pi r_s^2 \frac{dh_3}{dt} - \pi r_s^2 \frac{dh_2}{dt} = \pi r_d^2 U_d - \pi r_d^2 \frac{dh_2}{dt}, \quad (\text{B6})$$

and factorising gives

$$\pi r_s^2 \left(\frac{dh_3}{dt} - \frac{dh_2}{dt} \right) = \pi r_d^2 \left(U_d - \frac{dh_2}{dt} \right), \quad (\text{B7})$$

which we rearrange to find

$$r_s = \left[\frac{r_d^2 \left(U_d - \frac{dh_2}{dt} \right)}{\frac{dh_3}{dt} - \frac{dh_2}{dt}} \right]^{1/2}. \quad (\text{B8})$$

1001 Using Equation B8, the known hose radius ($r_d = 0.015$ m), the measured mean drill speed during PT2
 1002 ($\bar{U}_d = 8.82$ min⁻¹), and the rate of change in hydraulic head during PT2 ($dh_2/dt = 1.36$ m h⁻¹) and PT3
 1003 ($dh_3/dt = 7.40$ m h⁻¹), gives a borehole radius at the water-line $r_s = 0.14$ m. This estimate is double that
 1004 of the borehole model ($r_s = 0.07$ m; Table B1), but consistent with the borehole radius measured at the
 1005 surface.

1006 Measurements were not made of BH19g but BH19e had a radius at the surface of 0.17 m. As the pumping
 1007 test period was not recorded in BH19c and BH19e we assume that their near-surface radius was the same
 1008 as BH19g; that is, we assume $r_s = 0.14$ m for all response tests. Near-surface borehole radii larger than
 1009 predicted by the Greenler and others (2014) model could be explained by turbulent heat exchange from
 1010 warm upwelling water. Laminar flow is specified in the model. The effect of turbulent heat exchange on
 1011 borehole radius would decrease with depth so the model should perform better near the base. With no
 1012 better estimate available, we therefore use the model output for the borehole radius at the base (r_0 ; Table
 1013 B1).

Table B1. Borehole radii at the time of borehole breakthrough predicted using the model of Greenler et al. (2014) over ten depth intervals ranging from the ice surface to the ice-sediment interface at a depth below the ice surface corresponding to the ice thickness (H_i).

Depth (m)	Radius (m)		
	BH19c	BH19e	BH19g
0 – 100	0.07	0.07	0.07
101 – 200	0.05	0.06	0.05
201 – 300	0.06	0.07	0.05
301 – 400	0.06	0.07	0.06
401 – 500	0.07	0.07	0.06
501 – 600	0.07	0.07	0.06
601 – 700	0.07	0.07	0.07
701 – 800	0.08	0.08	0.08
801 – 900	0.10	0.10	0.11
901 – H_i	0.10	0.10	0.11
Mean	0.07	0.08	0.07

Supplementary Material for “Water flow through sediments and at the ice-sediment interface beneath Sermeq Kujalleq (Store Glacier), Greenland”

Samuel H. Doyle,¹ Bryn Hubbard,¹ Poul Christoffersen,² Robert Law,²
Duncan R. Hewitt,³ Jerome A. Neufeld,^{4,5,6} Charlotte M. Schoonman,^{2*}
Thomas R. Chudley,^{2†} Marion Bougamont²

¹Centre for Glaciology, Department of Geography and Earth Sciences, Aberystwyth University,
Aberystwyth, SY23 3DB, UK

²Scott Polar Research Institute, Cambridge University, Cambridge, CB2 1ER, UK

³Department of Mathematics, University College London, 25 Gordon Street, London, WC1H 0AY

⁴Institute of Theoretical Geophysics, Department of Applied Mathematics and Theoretical
Physics, University of Cambridge, Wilberforce Road, Cambridge CB3 0WA, UK

⁵BP Institute, University of Cambridge, Madingley Rise, Cambridge CB3 0EZ, UK

⁶Department of Earth Sciences, Bullard Laboratories, University of Cambridge, Madingley Rise,
Cambridge CB3 0EZ, UK

Correspondence: Samuel Doyle (sdd08@aber.ac.uk)

Introduction

The supplementary material includes two tables and four figures.

*Present address: Alfred Wegener Institute, Helmholtz Centre for Polar and Marine Research, Bremerhaven, Germany

†Present address: School of Natural and Environmental Sciences, Newcastle University, Newcastle Upon Tyne, NE1 7RU, UK

Table S1: Statistics and notes for the boreholes drilled in 2019. Note that the drill-indicated maximum depths underestimate actual depth as they do not account for the elastic extension of the hose under load, with a disparity for full-depth boreholes of 1-2%

Borehole	Date/time drilling started (UTC)	Max. drilling depth (m)	Notes
BH19a	2 July 2019 14:45	115.0	Abandoned
BH19b	2 July 2019 17:06	400.0	Geophone string
BH19c	4 July 2019 12:20	1031.0	Thermistor string, vibrating wire piezometer, and fibre optic cable
BH19d	12 July 2019 12:19	20.0	Seismic sparker
BH19e	12 July 2019 12:21	1013.3	Thermistor string and vibrating wire piezometer
BH19f	21 July 2019 11:12	180.0	Abandoned
BH19g	21 July 2019 16:39	1017.4	Current-loop pressure transducer

Table S2: Constants in the polynomial $y(t)$ of Equation 10 with error estimation.

Constant	Value
c_1	$+0.033 \pm 0.003 \text{ min}^{-1}$
c_2	$-0.27 \pm 0.02 \text{ min}^{-2}$
c_3	$+0.89 \pm 0.05 \text{ min}^{-3}$
c_4	$-1.40 \pm 0.07 \text{ min}^{-4}$
c_5	$+1.30 \pm 0.04 \text{ min}^{-5}$
c_6	$-0.09 \pm 0.01 \text{ min}^{-6}$
f_D	$+0.205 \pm 0.003.$

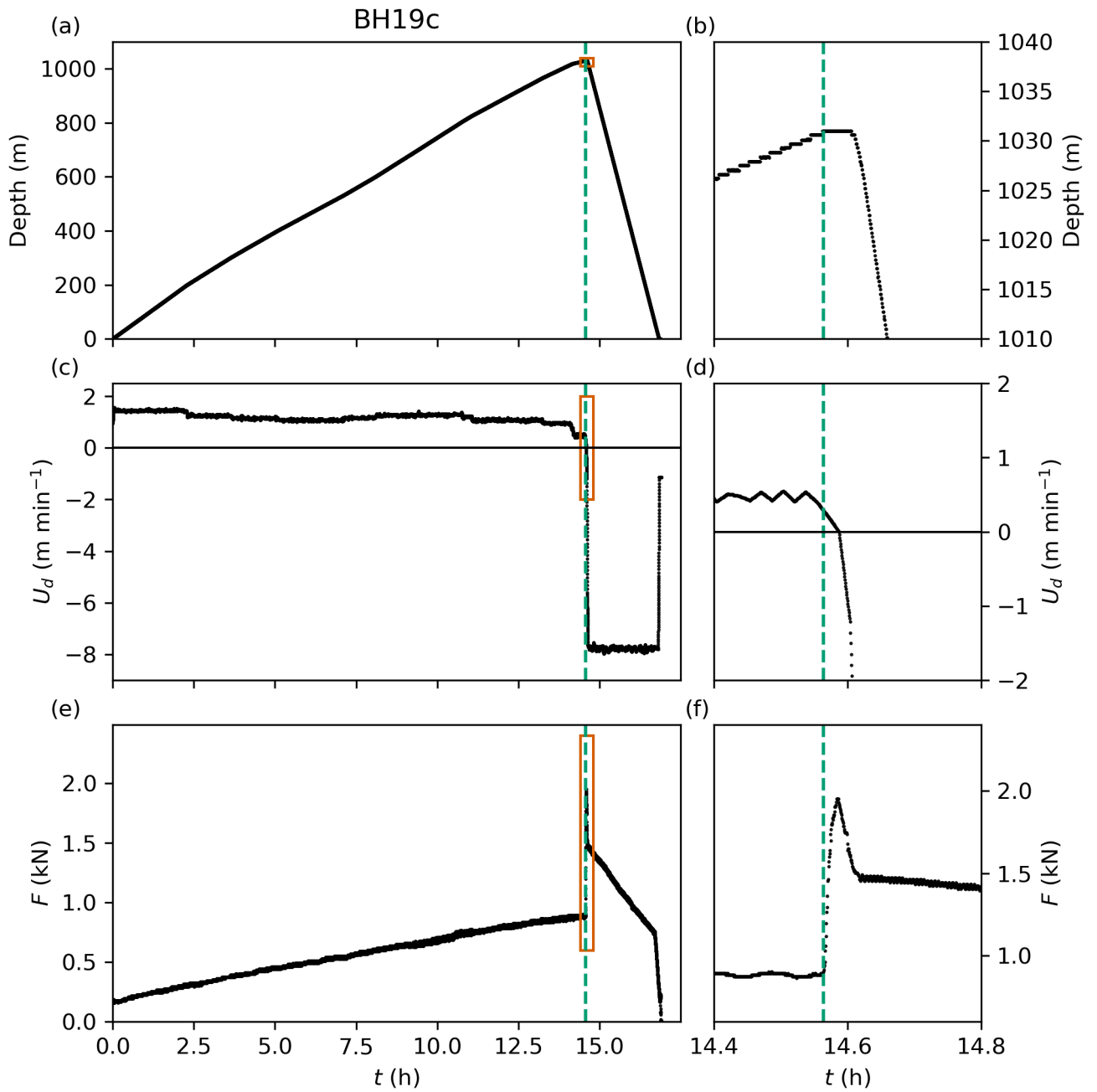


Figure S1: Time series of drill (a,b) depth, (c,d) velocity, and (e,f) force recorded on the drill tower during the drilling of BH19c. The extent of (b), (d), and (f) are shown by red outlines on (a), (c), and (e). Green vertical dashed lines marking the point of breakthrough.

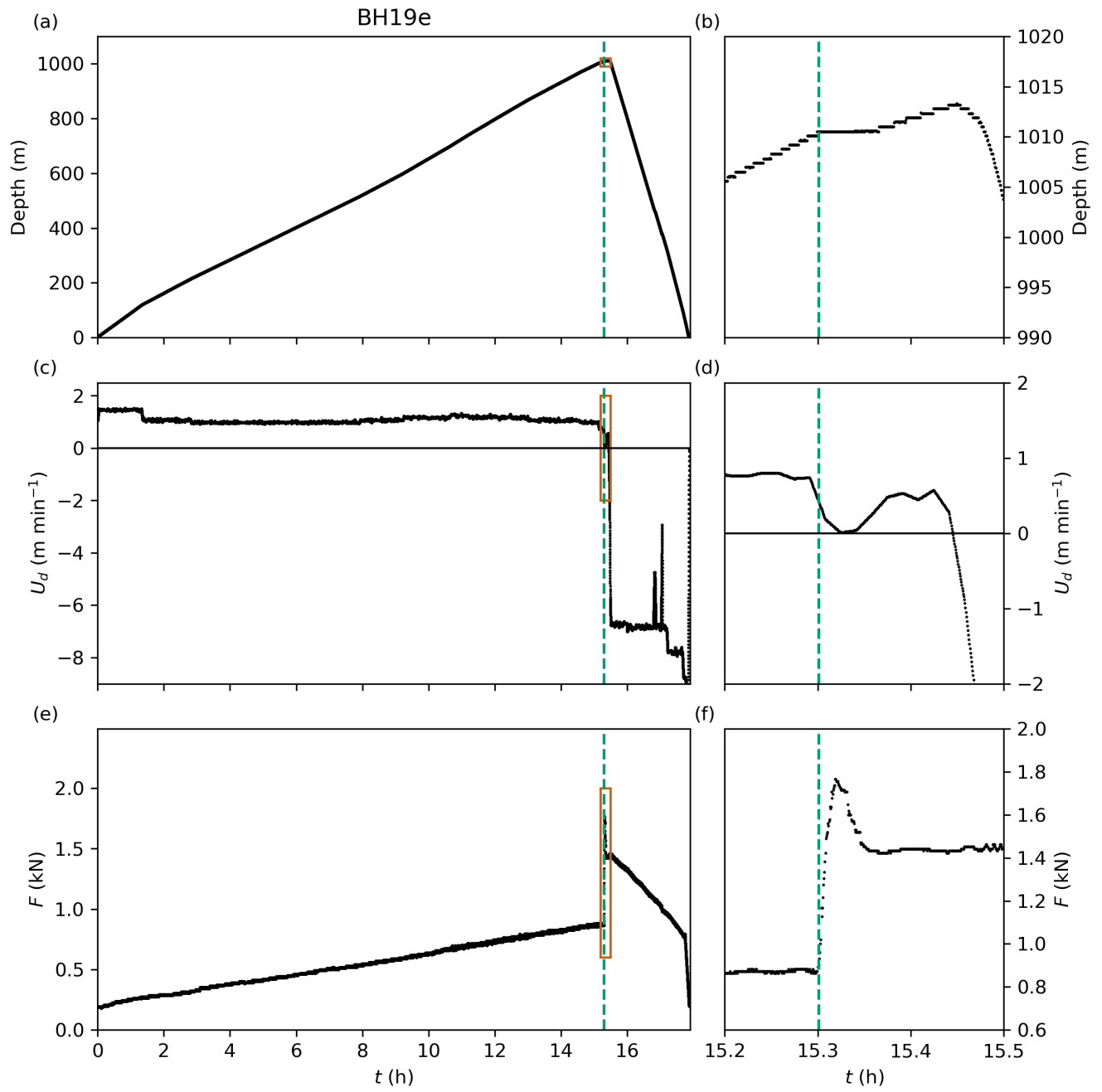


Figure S2: Plot of drill records for BH19e. See Figure S1 for a description.

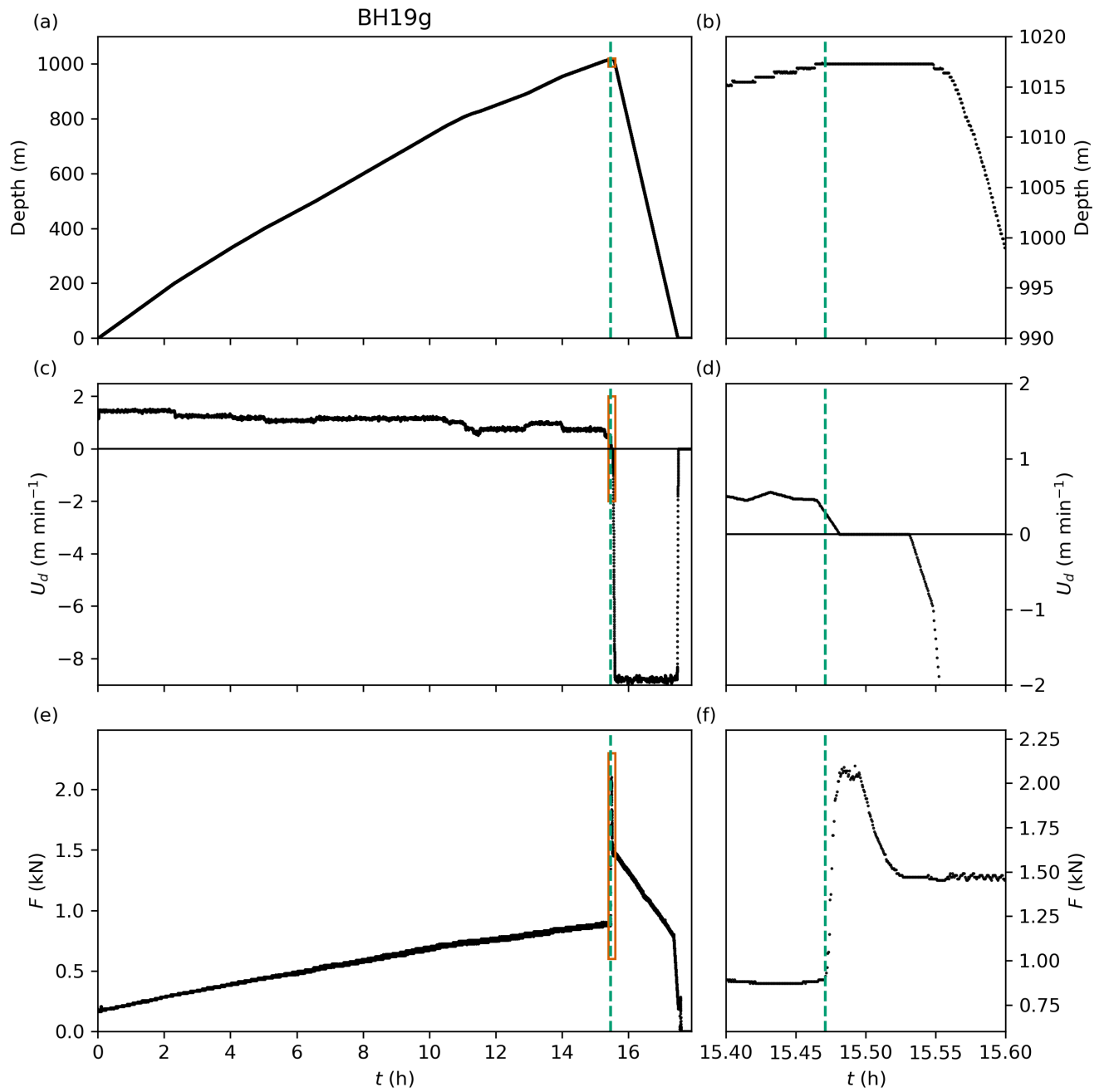


Figure S3: Plot of drill records for BH19g. See Figure S1 for a description.

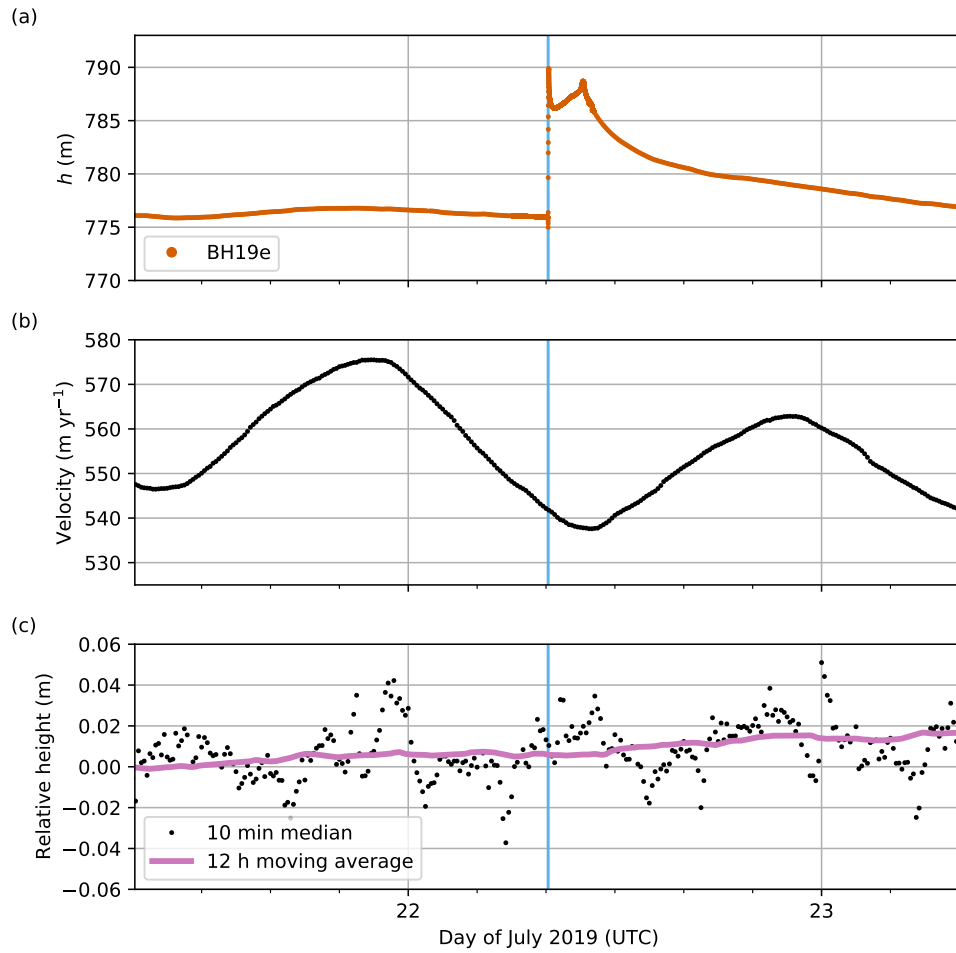


Figure S4: Time series of (a) hydraulic head in BH19e, (b) ice surface horizontal velocity and (c) relative surface height centred on the time of BH19g breakthrough, which is marked by the vertical blue line.